Sub-Shot-Noise measurement of spatially anti-correlated SPDC photons in the momentum plane of a Type I BBO using an EMCCD in the Photon Counting Regime

Panagiota Kardala

Masterarbeit in Physik
angefertigt im Institut für Angewandte Physik

vorgelegt der
Mathematisch-Naturwissenschaftlichen Fakultät
der
Rheinischen Friedrich-Wilhelms-Universität
Bonn

März 2023

I hereby declare that this thesis was formulated by myself and that no sources or tools other than those cited were used.

Bonn, 16.03.2023 .....

Date

.....

Signature

1. Gutachter: Prof. Dr. Sebastian Hofferberth
2. Gutachter: Prof. Dr. Simon Stellmer

Contents

CHAPTER 1

Introduction

The main research topic of my thesis is the description of an experiment that uses an EMCCD camera for the characterization of the spatial correlation in the momentum plane of a Type I BBO non-linear crystal used as an entangled photon source, in non-collinear geometry.

The primary research motivation is the exploration of the features provided by this EMCCD model for its future further application in imaging other non-linear phenomena.

Concerning the theoretical background, I shortly introduce the necessary to describe the SPDC process, the biphoton state in the momentum plane of the far field of the BBO, which is the light propagation inside a uniaxial birefringent crystal, the phase matching condition and finally how the biphoton angular profile is affected from the pump beam spatial properties. Further, the thresholding procedure is descibed in detail.

In the experimental analysis, I briefly describe the setup, the results of the figure of merit, of the Reduced Noise Factor and the correlation measure following two different ways of analysis.

CHAPTER 2

EMCCD camera

2.1 Operation

During the exposure time, photons impinging on the image sensor area are converted to 'photoelectrons' according to the quantum efficiency of the sensor in the photons wavelength. The photoelectrons contained in each pixel of the image area rows are vertically clocked downwards, first into the storage area and then into the 512-pixel serial register, row by row with the vertical shift speed chosen. If CCD mode is chosen, then the electrons are horizontally shifted to the conventional ADC output, according to the readout rate chosen. In Electron Multiplication (EM) mode operation, after the serial register, electrons are shifted towards the 536-pixel EM Gain register, where in each one of its stages a high-voltage clock (higher to vertical and horizontal) produces a multiplication of the photoelectrons through a process known as impact ionization. The average multiplication factor referred to as EM gain, is selected in the software from 4 to 1000.

Figure 2.1: EMCCD structure. [?]

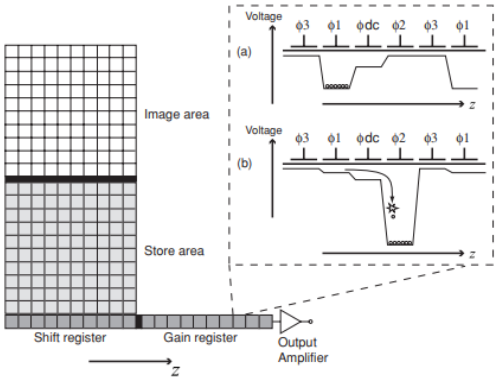

During the readout process, the signal of the multiplied electrons is converted into a voltage and finally is digitized by an Analogue to Digital Converter, where the output of each Analogue to Digital Unit (ADU) is presented as a 'count' in the signal intensity scale, corresponding to an exact number of electrons according to the sensitivity chosen (PreAMp). The counts sits on top of an electronic bias offset value, the so called 'baseline', where in the iXon Ultra 897 this is clamped at 100 counts in normal operation mode and 500 in EM. This is the reason that when measuring with the shutter closed, instead of a distribution of counts around 0, we obtain a mean distribution of 500 counts.

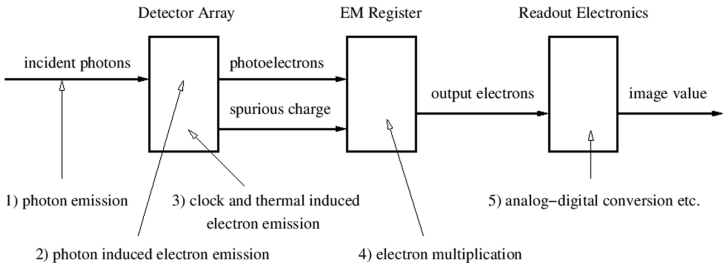

Figure 2.2: Image acquisition process with an EMCCD camera. [?]

Within the multiplication register, the electron shift Voltage from stage to stage is sufficiently high,

so that the probability an electron is accelerated until it has acquired energy larger than the bandgap in order to release extra energy to knock an electron out of a bound state is dramatically increased. This generated secondary electron will be trapped inside the pixel it was born in and it will be shifted together with the original electron to the next pixels, where both electrons are accelerated now until they have acquired sufficient energy for the creation of two pairs of electrons and holes.[**?**], [**?**] This repetition leads to a cascade of charge pair creation, an impact ionization where the probability of impact ionization per shift per electron p_c is low, 0.10 to 0.13 according to the gain choice, but due to the large number of n stages the resulting overall multiplication gain is given by $G = (1 + p_c)^n$, up to three orders of magnitudes. The EM amplification purpose is to increase the signal well above the readout noise, but the gain of the multiplication register is random due to the stochastic nature of the impact ionization events. Effectively, the number of input electrons is multiplied by the total EM gain G, defining the electric field applied, choosing $G = 1000$, for 1 electron input we would obtain a 1000 electrons output (rough estimation).

The measured counts can be expressed as

$$counts = \frac{\eta \cdot electrons \cdot gain}{preampsensitivity} + biasoffset$$

and the photons

$$photons = \frac{unbiasedcounts \cdot preampsensitivity \cdot \eta}{gain}$$

where η is the sensor quantum efficiency of the sensor to the impinging light wavelength. The EM output amplifier is similar to the conventional but is generally faster and hence suffers from increased read noise.

2.2 Noise sources

To calculate the probability of obtaining a number of counts from a pixel if light hits the sensor, we need a good description of the noise sources contribution. The first noise source originates from the photon emission itself. The second source is the quantum efficiency of the sensor, which is a stochastic process of converting a photon to electron or not. The third source stems of spurious charges and the fourth source is the excess noise introduced by the EM register. Finally, the output amplifier reading out the output electrons, creates the readout noise. The ADC introduces the so called quantization noise, due to the transformation of a continuous into discrete values, but is moderate and can be ignored.

2.2.1 Binomial photon absorption

The Binomial distribution describes processes with a given number of identical trials n with two random possible outcomes, either r successes with probability p and $n - r$ failures with probability $1 - p$. There are 2^n possible permutations of success and failure, of which the number with r successes is the number of ways of selecting r from n is ${}_nC_r = \frac{n!}{r!(n-r)!}$, the binomial coefficients. Thus the probability of successes is

$$P(r; p, n) = p^r (1 - p)^{n-r} \frac{n!}{r!(n-r)!} \tag{2.1}$$

with mean number of successes $< r >= np$ and success variance $\sigma_r^2 = np(1 - p)$. In the same manner we can consider the sensor's quantum efficiency, where a photon impinging on the sensor is either converted to an electron or not: each photon hitting the image section may cause the emission of a photoelectron with probability of success equal to the quantum efficiency q. Thus, the probability of obtaining n_e photoelectrons from n_p photons is given by the Binomial distribution (Eq:**??**) as

$$P(n_e, q, n_p) = q^{n_e} (1 - q)^{n_p - n_e} \frac{n_p!}{n_e!(n_p - n_e)!} \tag{2.2}$$

with mean number of successes $< n_e >= qn_p$ and variance $\sigma_e^2 = n_p q(1-q)$. [?] [?]

2.2.2 Excess Noise Factor

The downside of the multiplication process results from the statistical variation in the overall number of electrons generated from an initial electron by the gain register, due to the stochastic nature of the amplification, as described by Eq**??**. This uncertainty is called 'Excess Noise Factor' (ENF) and has been measured at $\sqrt{2}$ for EMCCDs, without reducing of course the detected electron number. One should multiply the Shot Noise by ENF when calculating the overall noise, because it has the same form as shot noise, since it increases the variation of the readout electron number around the mean value, in addition to the variation that already exists from the shot noise. Practically, it reduces the SNR by $\sqrt{2}$ as if the quantum efficiency of the sensor was half. A quite simple approach is to consider the EM register stages as a Poissonian light sources where the independent successful events are the duplication of an electron.

$$p(x \mid n) = \frac{x^{n-1} e^{-x/g}}{g^n (n-1)!} \tag{2.3}$$

where n is the input electron to the EM register, x the output multiplied electrons and g the overall EM gain. For an ideal electron multiplier, the output can be described as an exponential distribution in which the scale is the multiplication gain, when the probability of multiplication is low in every step.[?] The output is given by Eq **??**, where as illustrated in Fig **??** there is no one-to-one mapping between the number of electrons entering and leaving the multiplication register.

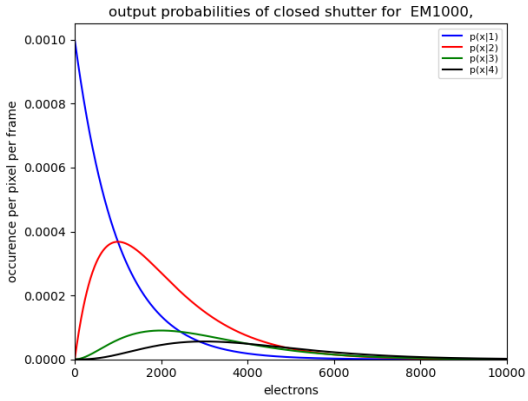

Figure 2.3: Eq**??** electron output probability for 1, 2, 3 and 4 input electrons.

The ideal distribution to describe the above process, would be Poisson distribution which describes cases where there are particular outcomes but no idea of the number of trials. If the average number of events within a time duration is known, one can calculate the probability of obtaining a particular number of events given the average number by taking the limit of the binomial distribution, in which the number of tries n become large while at the same time the probability p becomes small, but with their product constant. Supposing that on average λ events would be expected to occur in some interval, splitting this interval up into n very small equal sections such that the chance of getting two events in one section can be discounted i.e. like 2 photons impinging on the same pixel for really small exposure time, then the probability that a given section contains an event is $p = \frac{\lambda}{n}$. Now the probability that there will be r events in the n sections, is given by the binomial formula Eq **??** as

$$P(r; \lambda/n, n) = (\frac{\lambda}{n})^r (1 - \frac{\lambda}{n})^{n-r} \frac{n!}{r!(n-r)!} \tag{2.4}$$

As $n \longrightarrow \infty$ with r finite , the factorials give a power of n

$$\frac{n!}{r!(n-r)!} = n(n-1)(n-2)...(n-r+1) \longrightarrow \frac{n^r}{r!}$$

and an exponential appears

$$\left(1 - \frac{\lambda}{n}\right)^{n-r} \longrightarrow \left(1 - \frac{\lambda}{n}\right)^{n} \longrightarrow e^{-\lambda}$$

Inserting these two limits in the binomial distribution, we obtain the Poisson probability formula, describing the probability of obtaining r events if the mean expected number is λ

$$P(r;\lambda) = \frac{\lambda^r e^{-\lambda}}{r!} \tag{2.5}$$

The mean number of events is $< r >= \lambda$ and the variance $\sigma^2 = \lambda =< r >$. The total probability is $\sum_{r=0}^{\infty} P(r;\lambda) = 1$.

To calculate a series of Poisson probabilities it is convenient to start with $P(0;\lambda)$ and successively multiply by λ while divide by $1, 2, 3, 4..$, in order to get $P(1;\lambda)$,$P(2;\lambda)$,$P(3;\lambda)$...
$P(0;1) = P(1;1) = 0.368$.

For λ below 1, the most probable result is 0, explaining why $P(1)$ is decreasing monotonically and does not start from 0. For higher values of λ, a peak develops slightly below the mean (λ). Specifically, for integer λ, $r = \lambda$ and $r = \lambda - 1$ are equally probable.

The above behaviour is clearly illustrated in Fig **??** assuming that x axis is $r \cdot 1000$ and each peak a λ).[**?**]

2.2.3 Dark current

Another source of noise is the thermally generated electrons in the silicon, referred to as the dark current, strongly dependent on the sensor temperature and exposure time. It is considered negligible after cooling the sensor since it falls exponentially with cooling. Andor assures that for fast frame rate experiments and cooling below, 0C it can be ignored. Dark electrons are indistinguishable from photoelectrons, hence they are amplified in the gain register if existent. Thermal radiation is described by a Poisson distribution, so dark current is also a Poissonian noise source. Our camera spec sheet concerning the minimum dark current achievable indicates 0.0002 events per pixel per second, thus we will consider it negligible for exposures in the ms range.

2.2.4 Shot noise

Assuming the emission of photons produced in a coherent light source as individual independent emission processes, the emitted photon number n is a random variable with Poisson distribution, $P(n_p;\lambda)$ according to Eq:**??** with mean photon number $< n_p >= \lambda$ and $\sigma_p^2 = \lambda =< n_p >$. Hence, the probability of photons impinging the detector is Poissonian.[**?**] Photon shot noise is an inevitable source of noise. [**?**][**?**]

2.2.5 Spurious Noise

CIC

An electron generated during charge shifting is the Clock Induced Charge (CIC), a spurious noise source practically independent of exposure time and indistinguishable from photoelectrons during the amplification within the gain register.

I would like to point out here the difference between the creation origin of the thermal and CIC electrons. The silicon sensor surface is populated with holes that the thermally generated electrons can recombine with, before they reach the pixel well, counted as dark current. What generates the CIC is the movement of the holes during the vertical or horizontal transfer. Further, at low exposures CIC dominates while at longer the dark current. When using EMCCDs in single photon detection levels, what actually defined the detection limit is not the readout noise, but the CIC due to their indistinguishability with the true photons. Where are the CIC more likely to appear is extensively analysed in [**?**], where they proved that horizontal CIC dominates over vertical CIC. To eliminate the vertical and horizontal CIC probability when dealing with low photon flux, we shall choose the fastest vertical shift speed and highest readout rate. In photon

counting mode, if the EM gain is low photons are lost within the readout noise floor, so increasing EM provides better SNR on the cost of higher CIC level, due to the higher voltage required for higher EM gain. Our camera spec sheet concerning CIC indicates 0.00257 events per pixel. The output multiplied electron distribution probability caused by a CIC with generation p_{CIC} is derived from Eq **??** for 1 electron input, described by

$$p\left(x_{\mathrm{CIC}}\right) = p_{\mathrm{CIC}} p\left(x_{\mathrm{CIC}} \mid 1\right) = \frac{p_{\mathrm{CIC}} \exp\left(-x_{\mathrm{CIC}}/g\right)}{g} \tag{2.6}$$

EM register spurious noise

CIC can occur in the EM register, similarly to the other registers, where we will refer to it for simplicity from now on as serial CIC. There is literature proof where modelling the charge shifting and multiplication process, aiming to the calculation of the quantity and origin of the spurious charges, the best fit was found to correspond to 85% serial CIC and 15% CIC. These numbers are well expected since the chance for a spurious event is higher within the EM register where the Voltages are higher than any other sensor register. The serial CIC will suffer less amplification compared to CIC that travels the whole EM register and we have to account for the fact that can be born in any of the stages. Hence,the output distribution caused by a serial CIC with probability p_{ser} requires the summation accounting to each stage separately, expressed as

$$p\left(x_{\mathrm{ser}}\right) = \sum_{l=1}^{n} \frac{p_{\mathrm{ser}} \exp\left(-x_{\mathrm{ser}}/(1+p_{\mathrm{c}})^{n-l}\right)}{(1+p_{\mathrm{c}})^{n-l}} \tag{2.7}$$

Electron signal

The probability of getting n_e photoelectrons from a Poissonian light source (n_p) is given by a combination of mutually exclusive events of joint probabilities of the Poisson distribution(photons) and the binomial distribution(conversion), which is a Poisson distribution

$$p(n_e;\lambda,q) = \sum_{n_p=0}^{\infty} P(n_p;\lambda) P(n_e,q,n_p) = P(n_e;\lambda,q) = \frac{\lambda q^{n_p} e^{-\lambda q}}{n_p!}$$

with mean $< n_p >< n_e >=< n_p > q n_p$, the product of intensity and quantum efficiency.

The total variance of the image sensor signal is given by the total $\sigma^2 = \sigma_e^2 + \sigma_p^2$.[**?**]

Reflection, refraction, diffraction, scattering, absorption and electronic conversion, is a binomial selection process or a sequence of binomial selection processes. Thus, if the photons before the interaction are Poissonian, then they will be after the interaction as well.[**?**]

Readout noise

The readout noise is distributed according to a Gaussian curve centred on the value of the counts given by the baseline. Its width is defined by the readout rate, while it is not affected by the vertical shift speed, exposure or temperature.

$$P(x;\mu,\sigma) = \frac{e^{-\frac{(x-\mu)^2}{2\sigma^2}}}{\sigma\sqrt{2\pi}} \tag{2.8}$$

2.2.6 Sensor Non uniformity

All the scientific cameras to some degree exhibit blemishes which impair the faithful reproduction of the light signal, with primary source the sensor itself. Andor grades the standard cameras with the following definitions within the active image area which is defined as the central area ignoring the 2.5% of the pixels around the edge of the sensor, allowing following blemishes:

•Black Pixels are regions, typically pixels or small clusters of pixels, having less than 75% response than their neighbors, due to contamination on the sensor surface or embedded in the sensor. They are rarely a major issue unless they extend to many pixels (allowed 80 per million pixels-spec sheet 0).

•Hot Pixels have 50 times higher dark current than their neighbors, having different temperature response than the bulk of the sensor and so can appear to differing amounts at different temperatures. They are usually due to contamination embedded in the sensor (60 Per million pixels-spec sheet 0).

• Traps only occur in a single pixel and they temporary hold the charge, caused by contaminants getting into the CCD during the production process or by the effects of radiation on the CCD structure. As charge is shifted though a trap, it holds a portion of it(same as trap size) but while the trap is filled with subsequent charge the transfers are unaffected, thus, the charge in the trap slowly dissipates until it is refilled by new charge created by illumination or by new charge being shifted through the pixel. Traps can be of any size, minimum of single electron charge but they are only noticeable when it is greater than 200 electrons (4 Per million pixels allowed-spec sheet 0).

A combination of blemishes may adversely affect a column due to: a combination of more than 30 black or hot pixels, having a dark current greater than 2 times specification-Hot Column (allowed 1 Per thousand columns), having saturation less than 90% of the average column - Black Column (allowed 1 Per thousand columns), a trap.[**?**]

2.2.7 Dark histogram

As I will describe in the next section, when acquiring frames with the shutter closed, we can have a better understanding of the noise source contributions and the amplification process. In Fig **??** the counts obtain after different levels of EM gain applied is illustrated. When 4 EM is chosen, the output is governed by the gaussian distribution without any amplification. The larger the multiplication, the larger the amount of counts obtained. Hence, for 4 EM we have most of the counts sitting on the center of the read noise distribution. One can observe that the larger the EM the lower the distribution gets and spreads more towards higher number of counts, exactly as described for increasing electron input from the Eq **??**. In the extreme case of EM1000, the amplification tail exceeds the Gaussian head in height as expected. In this manner is technically illustrated how the photons emerge the noise floor.

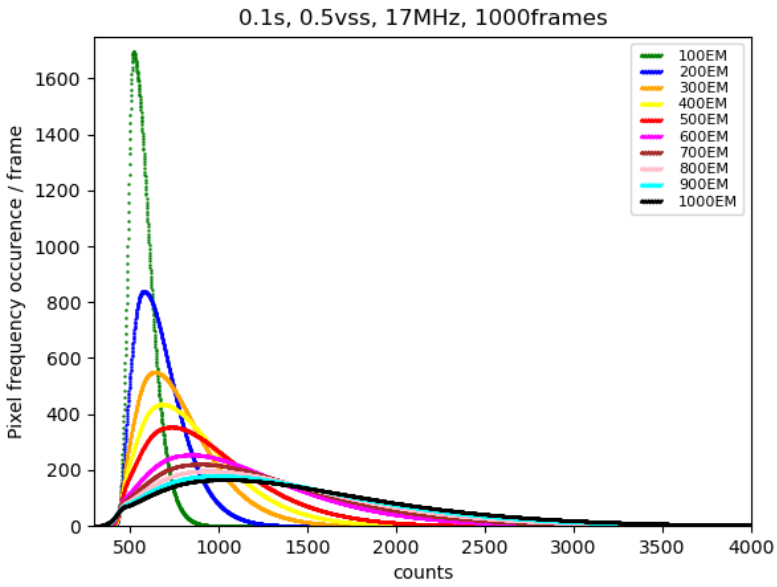

Figure 2.4: Output distribution plot of different EM application

Figure 2.5: closer look at **??**

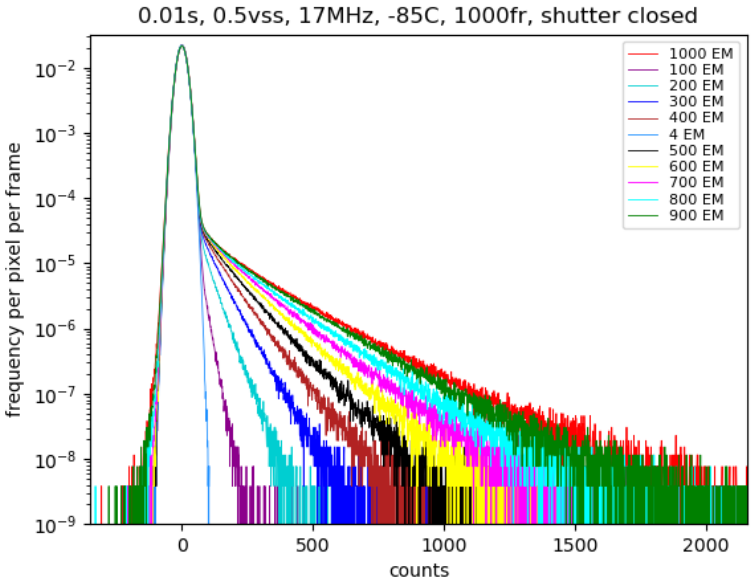

When the same output data are plotted in y-log plot axis, the tail amplified from EM is more evident allowing us to more accurately distinguish between the amount of amplified photons.

In these figures, there is no light impinging on the sensor so we observe CIC amplification. One would notice the sparce counts laying on the right side of the x axis, very high counts but very few of them, of the order of tens, most of the time reaching to the saturation limit. This is the effect of Cosmic rays that due to its high energy when entering the multiplication stage multiply much great that the common photoelectrons. There is an option for the Andor Camera, the cosmic ray filter, but it literally clamps the gain to really low values thus it was to use.

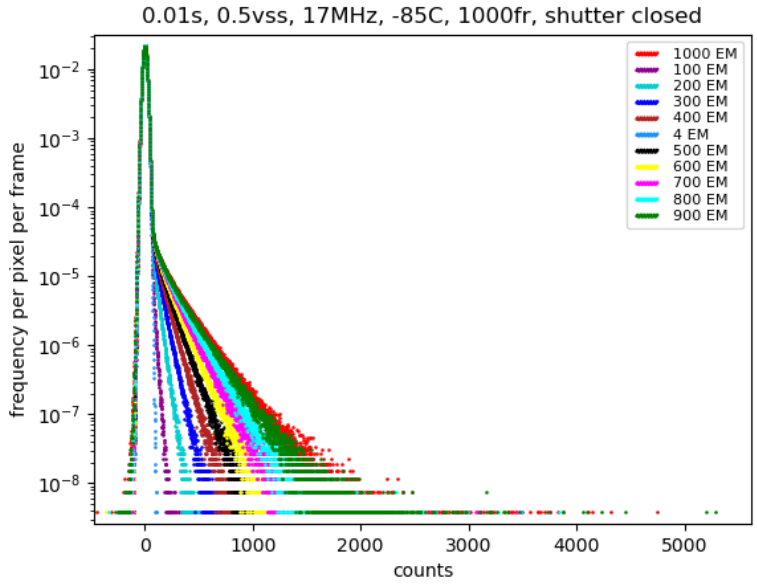

Figure 2.6: y-axis log output distribution plot of different EM application

Cosmic rays are so bright that we can still recognize them even after their averaging within 1000 frames. (Look carefully at)

CHAPTER 3

SPDC Theoretical Background

3.1 Introduction to SPDC

In spontaneous parametric downconversion (SPDC) a single input photon at higher frequency, called pump, after interaction with a nonlinear crystal splits into two of lower frequencies, called signal and idler. The SPDC process provides an entangled photon pair source with well-defined spectral and spatial properties, arising from the nonlinear crystal's optical dispersion.

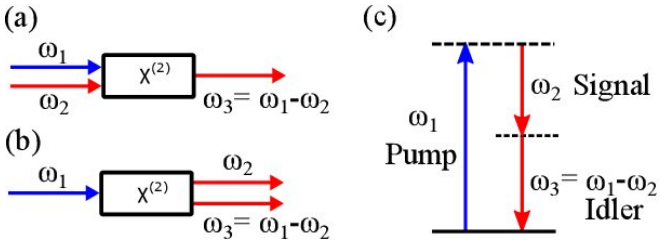

Figure 3.1: (a)Difference frequency generation process, (b)SPDC process, (c)SPDC energy level diagram.[?]

SPDC is a special type of difference frequency generation process. In the difference frequency generation, if a field at frequency ω_2 is present in the pump stimulates the difference frequency generation at $\omega_3 = \omega_1 - \omega_2$, resulting to a very efficient process called optical parametric amplification/oscillation, illustrated in Fig **??**a. If the frequency ω_2 is not present in the input, the generation of difference frequency at $\omega_3 = \omega_1 - \omega_2$ is still possible accompanied by the generation of frequency ω_2, where in this case the generation of the difference frequency is stimulated by the presence of the vacuum mode at frequency ω_2 in the input field and is therefore very inefficient (1 photon out of $10^5 to 10^{12}$ are converted). This second-order process of generating the frequencies ω_3 and ω_2 from the input frequency of ω_1 is referred to as the spontaneous parametric down-conversion Fig **??**b. [**?**] The term spontaneous refers to the fact that the process is stimulated by the vacuum mode at frequency ω_2 in the input field and the term parametric signifies that the total energy remains conserved during the process. I must stress here that SPDC is a linear function with the pump power, unlike Second-Harmonic generation or Difference-Frequency generation, since one pump photon splits into two photons but only one photon in each mode, so the dependence is clearly linear even though it is a non-linear process [**?**]. Figure **??**c represents the energy-level diagram of the SPDC process, in which the photon at frequency ω_1 gets absorbed and the absorber goes to a virtual state, finally decaying down to the ground state emitting photons at frequencies ω_2 and $\omega_3 = \omega_1 - \omega_2$. The energy and momentum conservation entangle the down-converted photons in energy-time, position-momentum, polarization, and angular position-orbital angular momentum. The emission directions of the downconverted photons are decided by the constraints imposed by the conservation of energy and momentum, referred to as the phase-matching conditions. [**?**]

When the SPDC photons propagate along the pump direction, we have collinear phase matching (Fig**??**a). Alternatively, in non-collinear phase matching, they propagate in directions non-collinear with

the pump where we have the so-called detuned phase matching (Fig**??**b).[**?**]

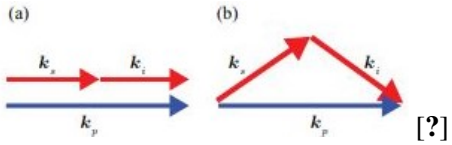

[**?**]

Figure 3.2: Phase-matching diagrams for the (a)collinear and (b)non-collinear emission geometries. [**?**]

3.2 Non-Linear Crystals

Assuming a non-magnetic medium that is not the vacuum, no external charges and currents, using Maxwell's equations we obtain the charge displacement due to an applied external EM field $\overrightarrow{D} = \epsilon_o \overrightarrow{E} + \overrightarrow{P}$. $\overrightarrow{P}$ is the induced polarization vector of the medium $\overrightarrow{P} = \epsilon_0 \chi \overrightarrow{E}$, with ϵ_0 the vacuum electric permittivity and χ the electric susceptibility of the medium. Depending upon the medium inversion symmetry, it is characterized as linear when it exhibits inversion symmetry and non-linear when it does not. In linear media, χ is a scalar independent of the direction along E is applied and $\overrightarrow{P}$ parallel to $\overrightarrow{E}$, whereas in a non linear medium χ is described by a tensor and $\overrightarrow{P}$ is not oriented parallel to the driving field, because the optical properties of anisotropic media are described by the Lorentz oscillator model, characterizing the restoring force acting on the electron cloud in different directions by different springs with a non-linear relation between the displacement and the driving field, leading to a non-linear relation between $\overrightarrow{P}$ and $\overrightarrow{E}$. Finally $\overrightarrow{P}$ is expressed according to the power series expansion of the applied EM field $\overrightarrow{P} = \epsilon_0[\chi^{(1)}\overrightarrow{E} + \chi^{(2)}\overrightarrow{E}^2 + \chi^{(3)}\overrightarrow{E}^3 + ...]$. The second order polarization term is described as $P_i^{(2)} = \epsilon_0 \Sigma_j \Sigma_k \chi^2_{(i,j,k)} \cdot E_j E_k$, where the second-order nonlinear susceptibility $\chi^2_{(i,j,k)}$ characterizes the medium's tendency to cause sum-frequency generation, difference-frequency generation, optical refraction etc, with $(i, j, k) = (x, y, z)$. Optically anisotropic crystals, so called birefringent, do not exhibit inversion symmetry and thus are characterized as non-linear crystals, since their anisotropy allows the manifestation of non-linear phenomena.

3.3 Birefringence

Birefringent materials' refractive index depends on the polarization and propagation direction of the light within them. In uniaxial birefringent media, the so called 'optical' axis is the direction governing the optical anisotropy, whereas all directions perpendicular to it or at a given angle are optically equivalent, i.e. rotating the material around the optical axis does not change its optical behaviour. A light beam with polarization perpendicular to the optical axis is governed by a refractive index n_0, called 'ordinary', while light with parallel polarization sees n_e, called 'extraordinary'. Technically, the refractive index of an extraordinary ray will always lay between n_0 and n_e, where the magnitude of the difference is quantified by the birefringence $\Delta n = n_e - n_o$, depending upon the beam direction, described by the index ellipsoid. If $\Delta n < 0$, the crystal is negative uniaxial. [**?**]

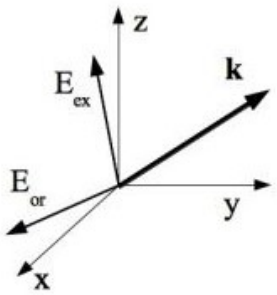

Figure 3.3: Ordinary and extraordinary polarization ray.[**?**]

The electric permittivity $\epsilon = (\epsilon_0)1 + \chi$ of an anisotropic medium which is a second-order tensor due to $\chi^2_{(i,j,k)}$, has a unique coordinate system (x, y, z) in which it becomes diagonal (ϵ_{xx}, ϵ_{yy}, ϵ_{zz}) in the corresponding coordinate axes e_x,e_y,e_z, that are called principal. If E is oriented along one of the principle axes, the electric displacement field D points in the same direction. The principal indices of refraction are given by $n_x = \sqrt{\epsilon_{xx}}$, $n_y = \sqrt{\epsilon_{yy}}$ and $n_z = \sqrt{\epsilon_{zz}}$. In a uniaxial crystal, the two principal refractive indices are equal to the ordinary $n_x = n_y = n_o$, while the third to the extraordinary $n_z = n_e$.

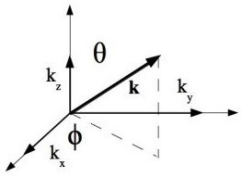

Figure 3.4: Propagation direction in spherical coordinates. [**?**]

For an incoming plane wave propagating inside a uniaxial crystal as illustrated in Fig **??** with electric field pointing in the k-z plane, after employing Maxwell's equations and deriving the dispersion relation, the extraordinary solution is described as $k^2(\theta) = \frac{k^2_{or}k^2_{ex}}{k^2_{or}\sin^2\theta + k^2_{ex}\cos^2\theta}$ where the extraordinary refractive index is obtained as

$$n^2(\theta,\lambda) = \frac{n^2_{or}n^2_{ex}}{n^2_{or}\sin^2\theta + n^2_{ex}\cos^2\theta} = \frac{1}{\left(\sin\theta/n_{ex,\lambda}\right)^2 + \left(\cos\theta/n_{or,\lambda}\right)^2} \tag{3.1}$$

indicating that the pump extraordinary refractive index depends on the phase-matching angle θ, formed by the optical axis and the pump propagation direction.

The dispersion relations providing the ordinary and extraordinary refractive indices for each wavelength are given by the Stellmeier equations, here for a negative BBO crystal,

$$n^2_o = 2.27405 + \frac{0.0184}{\lambda^2 - 0.0179} - 0.0155\lambda^2$$
$$n^2_e = 2.3730 + \frac{0.0128}{\lambda^2 - 0.0156} - 0.0044\lambda^2$$

where we see that for any wavelength, the ordinary wave propagates with larger refractive index than the extraordinary.[**?**]

3.4 Phase-Matching conditions

The phase-matching condition $\vec{k}_p = \vec{k}_i + \vec{k}_s$ with $\left|\vec{k}_p\right| = \frac{n_{p,}\omega_{(p\omega_p)}}{c}$, $\left|\vec{k}_i\right| = \frac{n_{(i,\omega_i)}\omega_i}{c}$, $\left|\vec{k}_s\right| = \frac{n_{(s,\omega_s)}\omega_s}{c}$, in the collinear configuration $\Delta k = 0$ where the angle between the signal/idler wavevectors with the

pump axis is $\theta_0 = 0$ requires $\frac{n_{(p,\omega_p)}\omega_p}{c} = \frac{n_{(s,\omega_s)}\omega_s}{c} + \frac{n_{(i,\omega_i)}\omega_i}{c}$, where in combination with the energy conservation equation $\omega_p = \omega_s + \omega_i$ of the degenerate case, we obtain for the Type I downconversion case that negative uniaxial crystals allow $e \longrightarrow o + o$,

$$n_{p,e}(\omega_p) - n_{s,o}(\omega_s) = \frac{\omega_{i,o}}{\omega_p}\left[n_{i,o}(\omega_i) - n_{s,o}(\omega_s)\right]$$

corresponding to $n_{ex}(\omega_{s,i}) = n_{or}(2\omega_p)$.
Finally the noncollinear phase matching geometry for propagation in the x-z plane ($\phi = 0$) with $\theta_0 \neq 0$, is given by

$$\left|\vec{k}_p\right| = \left|\vec{k}_s\right|\cos\theta_0 + \left|\vec{k}_i\right|\cos\theta_0 \Longrightarrow n(\theta)_p\omega_p = \cos\theta_0 n_s\frac{1}{2}\omega_p + \cos\theta_0 n_i\frac{1}{2}\omega_p$$

resulting to the non-collinear geometry detuned phase-matching condition $\Delta k = k_p(\cos\theta_0 - 1) \sim \theta_0^2 k_p/2$, that depends upon the crystal length L as well, because the larger the latter the bigger the phase mismatch can be.[**?**],[**?**] The downconversion efficiency is the highest in the collinear geometry with condition $\Delta kL < \frac{\pi}{2}$ which in its turn defines the maximum opening angle of the emitted photons from the pump propagation axis as $\theta_{0,max} \sim \sqrt{\frac{\pi}{Lk_p}}$, hence, the shorter the crystal the larger the divergence. I shall mention here that in the collinear geometry the phase matching condition is not truly 0 because there is practically always a slight detuning.

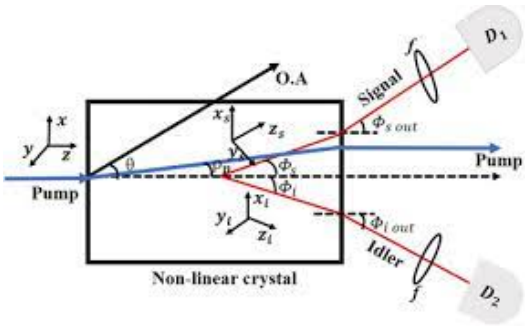

Figure 3.5: Notations ϕ_s,$\phi_{s,out}$,ϕ_i, $\phi_{i,out}$ represent emission angles for signal and idler beams both inside and outside the crystal. ρ_p is walk-off angle of pump beam inside the crystal and θ is the angle between the pump wavevector and optic axis. [**?**]

In both geometries, the pump will experience a spatial walk-off while it propagates as an extraordinary ray inside the crystal, translated as expecting the pump exiting the crystal face with a tilt from its original propagation axis. Assuming the coordinate system illustrated in Fig**??**, the spatial walk-off is in the +x direction, given by $\rho_p = \frac{-1}{n_e(\omega_{p,\Theta})}\frac{\partial n_e(\omega_{p,\Theta})}{\partial\Theta}\,|_{\Theta=\theta}$. [**?**].

3.5 Spatial entanglement properties of the SPDC momentum plane

In the degenerate wavelength downconversion case described above, due to the strong frequency anti-correlation expressed through $\int d\omega_s \int d\omega_i \delta(\omega_p - \omega_s - \omega_i)$ in the two photon amplitude expression, the latter becomes frequency independent when interference filter is used after the BBO to restrict $\omega_i = \omega_s = \frac{\omega_p}{2}$. [**?**]

Therefore, the quantum state describing the SPDC which is the vacuum state and the downconverted photons pair state

$$|\Psi\rangle \approx |\,\mathrm{vac}\rangle + \mu\iint \mathrm{d}\boldsymbol{k}_s^{\perp}\mathrm{d}\boldsymbol{k}_i^{\perp} f\left(\boldsymbol{k}_s^{\perp};\boldsymbol{k}_i^{\perp}\right)\left|\boldsymbol{k}_s^{\perp};\boldsymbol{k}_i^{\perp}\right\rangle, \tag{3.2}$$

is reduced to the expression of downconverted photon spatial degree of freedom, decoupled from the spectral degree of freedom. $\boldsymbol{k_s^{\perp}}$ and $\boldsymbol{k_i^{\perp}}$ are the transverse wave vectors, where the approximation

$\left|\boldsymbol{k}^{\perp}/k\right| \ll 1$ holds for all the modes because the signal and idler modes are usually at small angles to the longitudinal axis.[**?**] Assuming that the transverse section of the nonlinear crystal is much bigger than the pump beam diameter and the crystal's length L along the pump is small compared to the depth of the focus of the pump: the bi-photon amplitude is given by

$$f\left(\boldsymbol{k}_s^{\perp};\boldsymbol{k}_i^{\perp}\right) = \alpha\left(\boldsymbol{k}_s^{\perp}+\boldsymbol{k}_i^{\perp}\right)\phi_L\left(\boldsymbol{k}_s^{\perp}-\boldsymbol{k}_i^{\perp}\right) \tag{3.3}$$

$$\alpha\left(\boldsymbol{k}_s^{\perp}+\boldsymbol{k}_i^{\perp}\right) = \exp\left(-\frac{w_0^2}{4}\left|\boldsymbol{k}_s^{\perp}+\boldsymbol{k}_i^{\perp}\right|^2\right) \tag{3.4}$$

is the angular spectrum of the pump transferred to the biphoton state for a Gaussian pump beam profile with waist w_0.

$$\phi_L\left(\boldsymbol{k}_{\boldsymbol{s}}^{\perp}-\boldsymbol{k}_{\boldsymbol{i}}^{\perp}\right) = \operatorname{sinc}\left[\frac{L}{2}\left(\Delta k - \frac{\left|\boldsymbol{k}_s^{\perp}-\boldsymbol{k}_i^{\perp}\right|^2}{4k_{i,s}}\right)\right] \tag{3.5}$$

is the longitudinal phase-matching function given for the Type-I downconversion (same polarization biphotons) with $\Delta k = 2k_{i,s} - k_p$ for collinear phase matching and $\Delta k \sim \theta_0^2 k_p/2$ for non-collinear geometry.

The joint probability distribution in momentum is $P_m\left(\boldsymbol{k}_{\boldsymbol{s}}^{\perp};\boldsymbol{k}_{\boldsymbol{i}}^{\perp}\right) \propto \left|f\left(\boldsymbol{k}_{\boldsymbol{s}}^{\perp};\boldsymbol{k}_{\boldsymbol{i}}^{\perp}\right)\right|^2$.

The marginal probability distribution of each mode transverse k-vector is defined by $P_m\left(\boldsymbol{k}_u^{\perp}\right) = \int \boldsymbol{k}_v^{\perp} P_m\left(\boldsymbol{k}_u^{\perp};\boldsymbol{k}_v^{\perp}\right)$.

The conditional distribution is $P_m\left(k_v^{\perp} \mid k_u^{\perp}\right) = P_m\left(k_u^{\perp};k_v^{\perp}\right)/P_m\left(k_u^{\perp}\right)$. u, v represent s, i respectively or vice versa.

In the thin crystal regime and using a Gaussian approximation of the sinc function, the marginal and conditional distribution may be approximated as [**?**]

$$P_m\left(\boldsymbol{k}_u^{\perp}\right) \propto \exp\left[-\frac{2\gamma L^2\Delta k}{k_{i,s}}\left(k_u^{\perp}-\sqrt{k_{i,s}\Delta k}\right)^2\right] \tag{3.6}$$

with $\gamma = 0.193$

$$P_m\left(\boldsymbol{k}_v^{\perp} \mid \boldsymbol{k}_u^{\perp}\right) \propto \exp\left(-\frac{w_0^2}{2}\left|\boldsymbol{k}_u^{\perp}+\boldsymbol{k}_v^{\perp}\right|^2\right) \tag{3.7}$$

The marginal distribution expression **??** indicates that the emerging biphotons are distributed around cones centred on the pump propagation axis (not the walk-off direction), where their circular section has the same radius for signal and idler photons in the degeneracy. This ring represents the transverse momentum distribution of the degenerate downconverted photons. Inside this region the transverse momentum of the signal and idler are anticorrelated. If this anti-correlation were perfect, the photons would be found in diametrically opposite points inside the ring as illustrated in figure 5. However due to the uncertainty in the transverse momentum conservation, introduced by the finite pump beam spatial distribution, each generated photon is only localized to within the correlation area defined by the width of $P_{\mathrm{PDC}}\left(\boldsymbol{k}_v^{\perp} \mid \boldsymbol{k}_u^{\perp}\right)$

To map the transverse momentum $\boldsymbol{k}_v^{\perp}$ into the transverse position $\boldsymbol{r} = \frac{f}{k}\boldsymbol{k}^{\perp}$ in the plane of the used detector, we must perform a spatial Fourier with a $2f$ imaging system where the Fourier lens is placed in equal distances f from the detector and the crystal. Now the joint distribution of observing a photon at position $\boldsymbol{r}_s$ with its partner at $\boldsymbol{r}_i$ is

$$P\left(\boldsymbol{r}_s,\boldsymbol{r}_i\right) \propto P_{\mathrm{m}}\left(\frac{k_{i,s}}{f}\boldsymbol{r}_s,\frac{k_{i,s}}{f}\boldsymbol{r}_i\right)$$

the respective marginal distribution is

$$P\left(\boldsymbol{r}_s\right) \propto \exp\left[-\frac{2\gamma L^2 k_{i,s}\Delta k}{f^2}\left(r_s - f\sqrt{\frac{\Delta k}{k_{i,s}}}\right)^2\right] \tag{3.8}$$

same for the idler.

The latter equation yields a ring with a diameter

$$f\sqrt{\Delta k / k_{i,s}}$$

and width

$$f/(2L\sqrt{\gamma k_{i,s}\Delta k})$$

Finally, the conditional distribution is [**?**]

$$P\left(\boldsymbol{r}_s \mid \boldsymbol{r}_i\right) \propto \exp\left(-\frac{w_0^2 k_{i,s}^2}{2f^2}\left|\boldsymbol{r}_s + \boldsymbol{r}_i\right|^2\right) \tag{3.9}$$

the diameter (the full width at $1/e^2$ maximum) of the conditional distribution is

$$\Delta C \approx \frac{4f}{k_{i,s} w_0} \tag{3.10}$$

A cartoon setup illustrating all the above is given bellow

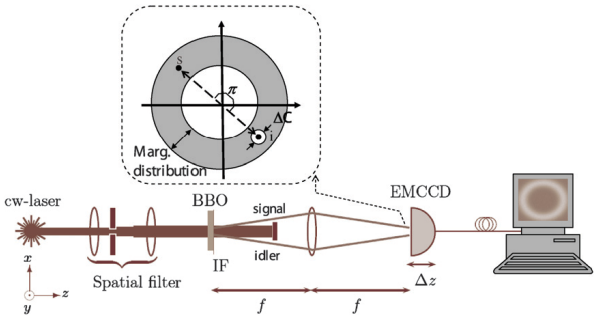

Figure 3.6: [**?**]

A fully detailed description can be found here [**?**], including the integration of Fresnel equation proving that we need a $2f$ configuration to access the momentum plane of the crystal.

3.6 Statistics of SPDC beams

Considering the pump beam as a continuous classic wave that exhibits no fluctuations divided into $N = T/\tau_r$ continuous segments with duration the transit time τ_r through the crystal, because each segment can be described by the Yurke-Potasek cavity formulation with $t = \tau_r$, will give rise to a Bose-Einstein distributed number of photons in each of the downconverted beams, that is left intact by the losses and the finite detector's quantum efficiency. The total photon number n generated in each beam during the counting time T is a sum of N independent Bose-Einstein random variables, resulting to a negative binomial distribution with mean $\overline{n} = \lambda T$, that is the sum of the individual means with variance $Var(n) = \overline{n} + \frac{\overline{n^2}}{N} = \overline{n}(1 + \lambda\tau_r)$. The quantity $\lambda\tau_r$ represents the mean number of photons emitted in a single transit time where $\tau_r = l/c$ is usually in the order of ps, hence $\lambda\tau_r \ll 1$ reducing the variance to $Var(n) \sim \overline{n}$, indicative of Poisson statistics. The above description implies that the mean

photon number emitted within a transit time is sufficiently small such that the probability of generating more than one photon is negligible, thus the overall sequence of photon emissions is consistent with a Poisson point process. If the pump exhibits phase fluctuations with coherence time τ_c, but is effectively sinusoidal during any transit time ($\tau_r \ll \tau_c$), the Poissonian statistics still holds but with lower mean value.[**?**]

From the integration of Eq **??** according to [**?**], the probability of detecting N_i photons in the area S_i if the anti-correlated photons are detected within area S_s with N_s, is expressed as

$$F(S_i) = \frac{< N_s N_i > - < N_s >< N_i >}{< N_s >}$$

where for $S_s = S_i$ we obtain

$$F(S_i) = F(S_s) = \frac{< N_s N_i > - < N_s >< N_i >}{(< N_s > + < N_i >)/2}$$

Since the statistics is Poissonian, the pairs are independent and their mean number equals their variance as

$$< N_i >=< N_s >=< N_s^2 > - < N_s >^2$$

yielding

$$F(S_i) = 1 - \frac{< (N_s - N_i)^2 >}{< N_s + N_i >}$$

the expression of the correlation peak between the two areas. For Poissonian pair statistics the correlation peak would be a positive value, hence indicate sub-shot noise correlations for the right hand side term. As described, even if the statistics of each photon separately is thermal, its variance reduces to the mean value because of maximum 1 photon per emission time segment.

CHAPTER 4

Sub-shot noise spatial anti-correlation measurement of BBO momentum plane with EMCCD

4.1 EMCCD as detector

For the measurement of the photons spectral degree of freedom, are required non-stationary optical elements and detectors with response time in the fs/ps range, where such devices are difficult to build. On the other hand, the photons spatial properties are easier to manipulate since elements with high spatial and angular resolutions already exist. There are numerous experiments where the spatial degree of freedom of single photons or entangled photon pairs has been measured, employing one detector for scanning the position where the photon is most probably to be found. In such a detection scheme the outcome of each measurement is binary, either having a photon hitting or not the detector, effectively reducing the usable dimensions of information. To access the full potential of the continuous spatial variable, a large array of detectors with single-photon sensitivity, sufficiently high quantum efficiency and spatial resolution with low noise shall be used.[**?**]

An EMCCD is a great device candidate, satisfying all those requirements. The measurement of the intensity of a light field depends on the ability to precisely count photons, a task quite cumbersome due to two reasons: firstly the shot noise, originating from the quantized nature of the electromagnetic field and secondly, the presence of losses in the detection process, no matter the detector used. Even for a perfect detector that would produce signal for each photon absorbed, the sensitivity of the light intensity measurement will be subject to the fundamental shot-noise limit. Even with the use of an EMCCD, we cannot accurately determine the exact photon number absorbed by its sensor due to the Excess Noise Factor. To circumvent the ENF, post processing methods such as Photon Counting, Thresholding, Multiple Thresholding, Bayesian Interference and Thresholding with Bayesian Interference are proposed, to accurately deduce the real input photon flux on a pixel from the digital readout. Operating the camera in photon counting settings with low photon flux $\ll 1$ with EM gain such that all the single photons emerge the noise floor, and imposing a threshold where above it we have a photoelectron event and below it noise:

if μ is the true mean number of photoelectrons accumulated in a pixel, the thresholding procedure would give in the abscence of false detections, a measured mean

$$m = 1 - p(0) = 1 - e^{-\mu} \tag{4.1}$$

with $p(0)$ the probability of detecting no photoelectrons. The left hand side indicates that after thresholding there is no ability of telling between one or more photon impinging on the sensor, while the right hand side indicates the Poissonian distribution of the thresholded 'binary' electrons.

The variance of Eq **??** is

$$\sigma_m^2 = m^2 p(0) + (1-m)^2[1-p(0)] = m(1-m) \tag{4.2}$$

smaller than the mean value m, as a result of the binary detection. Also, the variance of the difference is affected identically, hence taking their ratio, would yield an estimation of the quantum correlation of indipendent pairs with a standard quantum limit at 2. If the signal and idler positions are not in strict correspondance, the variance of the difference increases. [**?**]

The ideally perfect correlation in the bi-photon photon number is reduced also from the optical path elements towards the EMCCD and the sensor binomial absorption, so the overall effective quantum efficiency is lower than that of the sensor. Further, concerning to the uncertainty that determines the actual size of the coherence area in the far field, in order to collect all the correlated photons, the detection area $\mathcal{A}_{\text{det}}$ in an ideal situation must be larger than the coherence area $\mathcal{A}_{\text{coh}}$.

The total effective quantum efficiency η in terms of the detected correlated $\langle N_c \rangle$ and uncorrelated events $\langle N_u \rangle$ is defined as

$$\eta = \frac{\langle N_c \rangle}{\langle N_c \rangle + \langle N_u \rangle}.$$

The average number of all detected events $\langle N \rangle$ is equal to the sum of correlated $\langle N_c \rangle$ and uncorrelated $\langle N_u \rangle$ due to losses bright events, plus the detector's dark events $\langle N_D \rangle$. By substituting $\langle N_c \rangle$ with the number of detected biphotons $2\langle N_p \rangle$, we obtain

$$\langle N \rangle = \langle N_c \rangle + \langle N_u \rangle + \langle N_d \rangle \quad = \frac{2\langle N_p \rangle}{\eta} + \langle N_d \rangle$$

4.2 Noise Reduction Function

A number of studies based on the photon number spatial fluctuations of down converted pairs have been investigated using BBO type I and II crystals, exploiting the intensity correlations to experimentally demonstrate sub-shot noise statistics.([**?**], [**?**]) Photon number counting is a phase-insensitive intensity measurement. Non-classical Gaussian states, such as the squeezed vacuum state generated by SPDC, is entangled in the photon number, meaning that two ideal detectors intercepting each modes respectively always measure the same number of photons. This correlation is strongly nonclassical and does not involve any measurement of the phase.[**?**]

The spatial correlations between the signal and idler photons have two origins: the quantum, because photons are emitted by pairs, and the classical, because of the non spatially stationary nature of the intensity, where the mean intensity in the far field follows the phase-matching profile. [**?**] The quantized nature of the electromagnetic field sets the classical limit to the sensitivity of the spatial measurements of correlated photons.

Generally, the quantity of variance indicates the magnitude of spread of the measured data around its mean value. For a coherent state, the anticipated error in estimating the photon number difference is given according to Poissonian statistics as

$\left\langle \Delta^2 (A-B) \right\rangle = \langle A+B \rangle$, defining the so-called Shot Noise Limit (SNL).

The variance of the photon pair number difference in the far field normalized to the shot noise is expressed as

$$r = \frac{\left\langle \Delta^2 (N_1 - N_2) \right\rangle}{\langle N_1 + N_2 \rangle} = 1 - \eta \tag{4.3}$$

with η the overall quantum efficiency of the detection described above. r is usually refereed as 'degree of correlation' or most commonly 'Noise Reduction Factor'. Sub-shot-noise sensitivity in the measurement is achieved if $r < 1$.

Multiple papers state sub-shot noise correlation measurements withing the last decade, in a recent one, the authors of [**?**] explicitly state measurement of sub-shot-noise statistics in far-field measurements of Type II BBO, using the normalized variance expression on binned pixels after background subtraction and thresholding, with value $r = 0.88 \pm 0.09$, while they verified that images issued from different laser shots do not exhibit such a sub-shot noise behaviour, since for these images, $r = 1.02 \pm 0.12$ both in the near-field and the far-field.

Another approach to observe the sub-shot noise statistics, as described in the previous Section(3.1), is calculating the ratio of the mean 'binary' photon variance (Eq. **??**) to the variance of the number difference of spatially opposite pairs. The authors of [**?**], using an EMCCD and a Type I BBO, employed such an analysis dividing the recorded images of the spatial representation of the momentum plane in the camera, in opposite angular sectors. They satisfied every necessary condition for clear correlation resolution, using a wide beam radius, thresholding with appropriate exposure time and using filters to narrow the emitted wavelengths around degeneracy. Even a perfectly phase matched crystal would still produce biphotons within a narrow wavelength band, where each wavelength pair would suffer different refractive index until exiting the crystal, thus would exit towards different directions shifted away from the original pump direction propagation. All the different wavelength pairs have the same diameter, including the coherence area uncertainty, an elegant way of surpassing these widening parameters is choosing wider areas to calculate their difference, hence the sectors. They chose a number of $S = 180$ sectors, i.e. 90 opposite pair areas, where each sector correspond to a detection area of 2 pixel width, double their coherence area, which is proved to give good resolution. The sector length is defined from the inner radius up to almost 50 pixels width.

The photon number difference between two opposite sectors is defined as

$$\sigma^2_{\text{diff}} = \frac{1}{S/2-1} \sum_{i=1}^{S/2} \left(n_i - n_{i+S/2} \right)^2 \tag{4.4}$$

and dividing this quantity either by the mean number of photons in a sector

$$n_{\text{moy}} = \frac{1}{S} \sum_{i=1}^{S} n_i \tag{4.5}$$

or by the
variance of the photon number in a sector

$$\sigma^2_s = \frac{1}{s-1} \sum_{i=1}^{S} \left(n_i - n_{\text{moy}} \right)^2 \tag{4.6}$$

The correlation measure can be expressed as

$$r = \frac{\sigma^2_{\text{diff}}}{n_{\text{moy}}} \tag{4.7}$$

either

$$r' = \frac{\sigma^2_{\text{diff}}}{\sigma^2_s} \tag{4.8}$$

where a mean value plus 2 STDs well bellow 2, will yield subshot noise correlations. Since the variance of the photon number will always be smaller than the mean photon (Eq **??**), r' will give larger values compared to r, but the reason that it is considered more accurate than r is because both variances are affected by the binary detection in the same way, thus their ratio will provide a more accurate estimation of the quantum correlation measure.

In this figure of merit the minimum value expected is defined from the overall quantum efficieny as in , doubled, because each sector is considered as either an idler or a signal photon, not as the average of Eq. **??**.

CHAPTER 5

Modelling the EMCCD noise

To obtain the CIC, serial CIC and Readout contribution that lead to a non zero output in the absence of illumination on the sensor, from experimental data of dark frames with closed shutter, I implemented two different functions, in order to calculate the threshold for photon counting mode accurately.

The three different noise sources contribute to the probability distribution as illustrated bellow, where blue indicates the readout Gaussian distribution, green the serial CIC output and blue the CIC output, on the data used for the modelling. The bias offset was deduced from the data to obtain the real counts, meaning that the Readout curve was centred at 0.

Figure 5.1: Representation of the noise sources contribution on dark frames

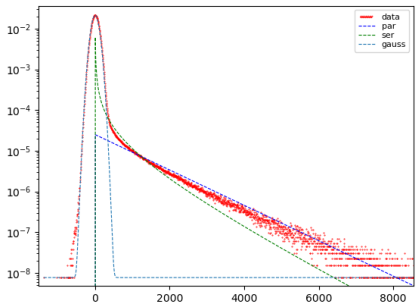

In the first case a convolution of the three noise probabilities described in Section(1.2.2) was employed exactly according to [**?**] using an existing Matlab script (author Ivan Migorodesky)

Figure 5.2: Convolution of the three noise probabilities according to [**?**], 0.0001s, 17MHz, 0.5vss, -85C.

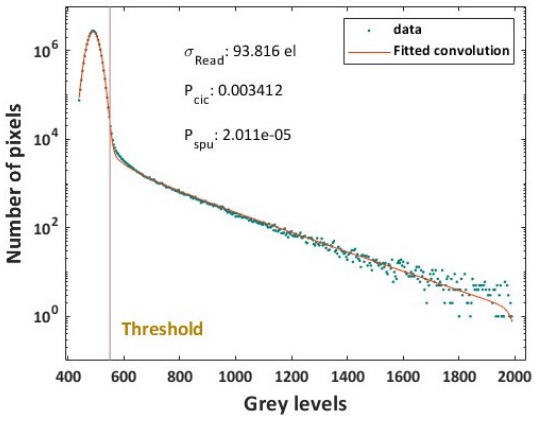

I have to stress here that this script assumes $p_c = 0.01$ and m=596 stages in order to obtain g=1000.

The camera has instead 536 stages and $pc = 0.01297$ is required to assimilate EM 1000.

Secondly, as described in [**?**] using an analytic approximation, where they approximate CIC and serial CIC as Poissonian events (**??**) thus assuming possibility of maximum only 1 possible CIC per pixel P_p and serial CIC arising only in one of the EM stages with very low probability P_s, derive the total distribution probability, where we either have one of the CIC events or none as outcome, described by

$$P(n) = \int_0^n \left[\left(1 - p_{\text{CIC}} - m p_{\text{ser}}\right) \delta(x) + \left(\frac{p_{\text{CIC}}}{\gamma} e^{-x/\gamma} + \sum_{k=1}^{m} \frac{p_{\text{ser}}}{\gamma_{m-k}} e^{-x/\gamma_{m-k}} \right) H(x) \right] - \mathcal{N}(n - x, \sigma) dx \tag{5.1}$$

with m the number of stages, $N(n, \sigma)$ the Gaussian distribution of the readout noise, $H(n)$ the Heaviside function and n the output electron number.

Because this expression is a mixture distribution of a zero output in the case of no spurious electron and an exponentially distributed output in the case of a spurious electron, convolved with the read noise, since the EM gain is assumed high for photon counting mode measurement, the convolution of the Gaussian with the exponential distribution is ignored since the exponential width of the read noise is much smaller than that of the CIC, finally reducing to

$$P(n) \approx \left(1 - p_{\text{CIC}} - m p_{\text{ser}}\right) \mathcal{N}(n, \sigma) + \left(\frac{p_{\text{CIC}}}{\gamma} e^{-n/\gamma} + \sum_{k=1}^{m} \frac{p_{\text{ser}}}{\gamma_{m-k}} e^{-n/\gamma_{m-k}} \right) H(n) \tag{5.2}$$

The Heaviside function is required because no negative values are allowed to enter the exponential distribution, since they are defined for electron input number larger than 1. Implementing the above function on the dark frames with closed shutter for 0.0001s exposure in kinetics mode with 17MHz readout rate and $0.5\mu s$ vss at 1000 EM gain, I obtain the total noise probability distribution

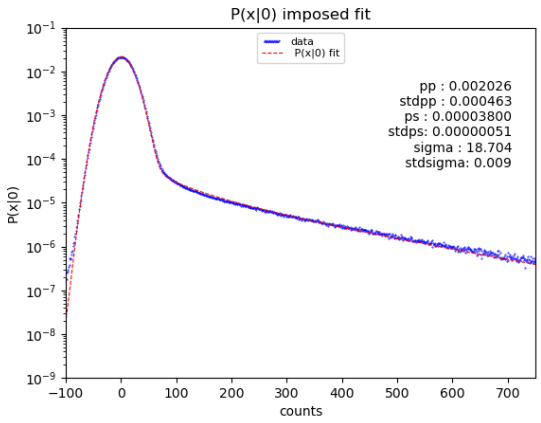

Figure 5.3: Additive contribution of the three noise probabilities according to [**?**], 0.0001s, 17MHz, 0.5vss, -85C.

The above fit verifies that we can approximate the three noise source as additive, without the need of a total convolution. The readout noise is added after the EM multiplication and the two spurious event happen independently.

Now comparing the two methods results, we obtain similar values but not identical. In the first method the gaussian variance is larger at $\sigma_c = 19.1$ counts while in the second at $\sigma_a = 18.7$, where fitting only a normalized gaussian contribution to the histogram gives the latter result, thus i can say is slightly more accurate. Concerning the CIC probability in the first case is $p_{CIC,c} = 0.0034$ while the second $p_{CIC,a} = 0.0020$. Andor states that in the lowest exposure in 0.3vss after thresholding the number of spurious events is at 0.00257, thus i would say that the second method underestimates the CIC probability. Finally, $p_{ser,c} = 2.0 \cdot 10^{-5}$ $p_{ser,a} = 3.8 \cdot 10^{-5}$, where the second is closer to the data, because if one looks carefully at the convolution tail the serial contribution curve is not

properly tailored as in the analytic formula plot. Concluding on p_{cic}, I cannot be adamant about the accuracy on the height of the multiplication tail derived from the convolution formula for more stages and lower duplication probability, but it is indeed closer to the spec sheet value. I have to stress here that concerning the second method one has to perform a very careful tuning of the p_{ser} while imposing the fit, because if defined higher than its true value the green spike emerges above the Gaussian curve center.

To obtain the optimum threshold value for analysis in photon counting mode where above a defined threshold we assume that the event signifies one photoelectron and below it the noise, to avoid the excess noise uncertainty , according to the paper [**?**] used for the first method described above, a multi-imaging strategy is proposed by taking into account the possibility of multiple photodetection events on 1 pixel, based on Bayesian estimation on each image, with a priori information given by the sum of the images. Because the relative contribution of the noise increases on decreasing photon flux per frame in photon counting mode, since the CIC noise is dominating, an optimum level of illumination is necessary for which the total error due to both multiple-photon and noise-induced fake detections is minimal. Both the optimum illumination level and the threshold are obtained from the minimizing of error caused by all the fake detections, for each independent pixel, due to the inhomogeneous sensor response that yields different results for the same illumination. The thresholding procedure is as follows:

The mean light level per pixel on each frame is assumed << 1 and there is an input photon $y = 1$ if the output x in grey levels/ unbiased counts is greater than the defined threshold $x > T$. Alternatively if $x < T$, there is no input photon and the result of the procedure gives $y = 0$.

The false detections events leading to errors are the following:

1) $x > T$ for $n = 0$, due to noise one photon is detected instead of 0, with probability $p(y = 1 \mid 0) \equiv p_{10}$.

2) $x < T$ for $n = 1$, due to random gain 0 photons are detected instead of 1, with probability $p(y = 0 \mid 1) \equiv p_{01}$.

3) $x > T$ for $n = 2$, where 1 photon is detected instead of 2 with probability $p(y = 1 \mid 2) \equiv p_{12}$. The case $x < T$ for $n = 2$ is considered negligible.

The approximate light level $\mu = \langle n > /N$ needed on each frame for a mean photon number $\langle n \rangle$ on the sum, can be obtained according to the number of frames N recorded.

The repartition functions of the conditional probabilities of errors are described as:

$$p_{01} = \sum_{x=0}^{T} p(x \mid 1) \tag{5.3}$$

$$p_{10} = \sum_{x>T}^{\infty} p(x \mid 0) \tag{5.4}$$

$$p_{12} = \sum_{x>T}^{\infty} p(x \mid 2) \tag{5.5}$$

with $p(x \mid 1)$ and $p(x \mid 2)$ defined from **??**, while $p(x \mid 0)$ is the experimental probability distribution derived from the closed shutter histogram fits above.

Considering $T/g << 1$, Eq **??** reduces to $p_{01} = 1 - e^{-T/g} \cong T/g$, while **??** can be approximated as $p_{12} \cong 1$.

$$Q = N\left[p_{01}\mu + p_{10}(1-\mu) + p_{12}\frac{\mu^2}{2}\right] =< n > p_{01} + (N- < n >)p_{10} + \frac{< n >}{2N}p_{12} \tag{5.6}$$

The minimization of the quadratic error Q with respect to variables N and T, for one pixel on the sum

of the images, assuming equal weighting of the false events, with $N- < n > \approx N$, leads to

$$\mu = \frac{< n >}{N} = \sqrt{2p_{10}} \tag{5.7}$$

and T such as that

$$p_{10} = \frac{g^2}{2}\left(\frac{\partial p_{10}}{\partial T}\right)^2 \tag{5.8}$$

The value of μ can be obtained for given T through the sum evaluation of Eq **??** using the dark frames histogram. To calculate T, the above derivative is evaluated by calculating p_{10} for each value of T so to calculate progressively the finite differences $\left(p_{10}(T+1) - p_{10}\ (T-1)\right)/2$.
Finally for both the convolution fit and the analytic fit, the plotted derivative yielded a minimum at 60 counts. Even though the fitted probabilities were not identical. What practically defines the threshold is the Gaussian variance, where usually most of the thresholding schemes assume $2.8\sigma < T < 3.2\sigma$ without performing all the above procedure. In the analytic case $T = 60 = 3.21\sigma_a$ and for the convolution $T = 60 = 3.15\sigma_c$. I have to mention here, that concerning the SPDC momentum correlations, overestimating the threshold by 1 or 2 counts gave no difference.

The authors of [**?**], referring to this thresholding procedure described above, present a clear graphical method for the threshold and optimal light level estimations, employing the simultaneous graphical visualization of the three probabilities involved in the detection errors on 1 pixel, hence deriving in a straightforward, the threshold level and thus the best mean level of illumination to be used in order to minimize the false detection probabilities that might ruin the real image statistics.

Considering as before: $\mu \ll 1$ and Poissonian light distribution, the above mentioned probabilities in the single photon counting regime are $p(x \mid 0)(1-\mu)$, $p(x \mid 1)\mu$ and $p(x \mid 2)\mu^2/2$, corresponding to the probability of recording only noise in the absence of light, output for 1 input photon when there is light and then for two photons while illumination, respectively. Here, as in the analytic method, we have to divide the pixel frequency occurence by the number of total pixels along the frames, to normalize the y axis according to probability described by Eq **??**.

The probabilities $p(x \mid 0)(1-\mu)$ and $p(x \mid 1)\mu$ associated respectively with the detection of x grey levels for 0 and 1 input photons, have an intersection point at x_{inn1}, increasing for decreasing input mean photon number, with limiting point incide the CIC region for $\mu \longrightarrow 0$.

Along with each threshold calculation we can derive the false detection probabilities for an overestimated or undervaluated level of light compared to the one used for the threshold calculation.

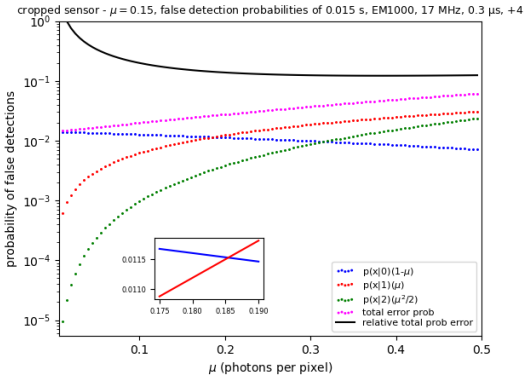

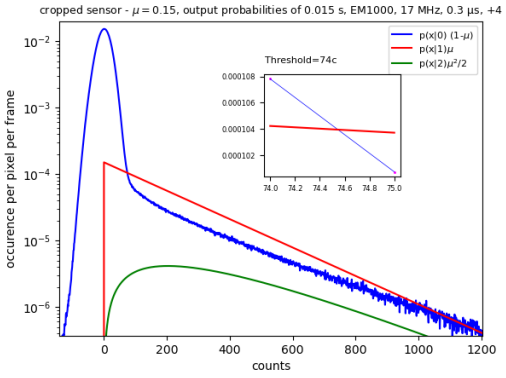

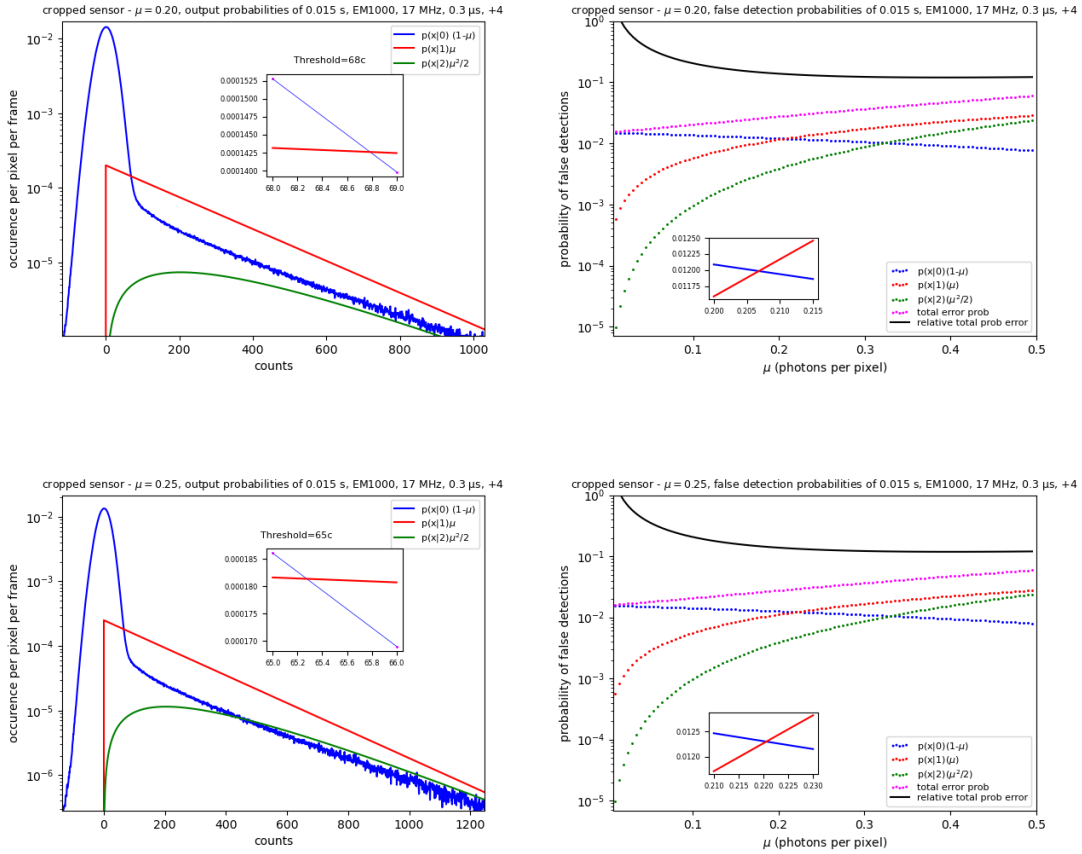

We can easily observe that for increasing assumed light level, higher than the one used for the threshold calculation, the necessary threshold lowers in counts. The $p(x \mid 2)\mu^2/2$ curve generally remains below the $p(x \mid 1)\mu$ curve, but crosses the probability $p(x \mid 0)\ (1-\mu)$ for a value of grey levels $x = x_{\text{int }2} > x_{\text{int }1}$.

μ is treated as a parameter here to obtain the threshold according to it and not only due to the dark noise histogram.

I need to mention here, that the histograms raw data used bellow are after cropping to the same size as the SPDC images, where since I am not using the whole sensor area there is no need to include uniform edge non uniformity which is inevitable because it is attached to a Peltier cooling, hence we observe the heat transfer gradient in a manner.

The same analysis was repeated for μ0.010s exposure time and 0.015 s, where for 0.010 s I obtained the same threshold as in the two previous methods. The obtained thresholds were used for the different exposures times I had in my measurement data concerning the correlation scheme.

The analysis of more thresholding techniques can be found in detail here [**?**].

Finally, if one wants to calculate the mean sensor response function can employ [**?**]

$$I_n = PreAmp\left(gn + \mu + p_{cic}g + p_{ser}\frac{g-1}{p_c}\right) \tag{5.9}$$

CHAPTER 6

Analysing the experimental Data

The primary experimental goal was to reproduce the approach proposed in the paper [**?**], where they demonstrate the capability of an EMCCD camera to record multiple SPDC coincidence events with mean photon number per pixel much higher than 1, contrary to the usual approach performed in photon counting regime, hence providing a mechanisms for recording quantum signatures for bright correlated photon sources. My results are exactly opposite from their suggestion, thus we had to implement another approach to investigate if the setup itself was responsible for the great discrepancy of the results. Having already assessed the camera operation in the photon counting regime, the method implementation of [**?**] was possible, where the identical setup and existing measurements at the low exposure times required were used, to analyse the data accordingly.

6.1 Experimental Setup

Figure 6.1: experimental setup

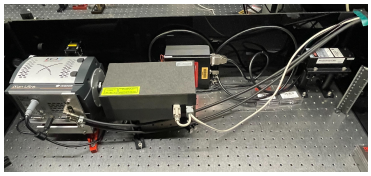

For the proper photon detection, our system was optimized by minimizing the background light with a custom made light-tight pvc box enclosing the EMCCD, the f=25.4mm Fourier lens and the SPDC source. The SPDC photon source used is the box was contained in the ”qutools' Entanglement Demonstrator”. The box contains a laser source emitting a 405 nm vertically polarized beam, aligned through a mirror to impinge on a half waveplate, and a polariser for choosing $|V\rangle$ or $|H\rangle$ laser polarization. The laser beam is focused on two glued BBO crystals with their optic axes crossed, each 0.6mm thick. Tje lens is tighty fitted on a post between the box filter and the premium 800 nm mounted in the camera entrance.

All the measurements were performed with Horizontal polarization where the respective crystal is more efficient to. Finally the box is cover by a carton with a thick premium filter attached on it with wavelength band at ±3nm, center at 812 nm. A 400nm premium filter is placed directly after the laser exit because I found out that it emits light at higher wavelengths, using the EMCCd camera. I would not have known, unless that was not the case with the laser used prior, it was leaking light close to 800nm and we found out after trying with multiple filters combination to avoid the case of fluoresce.

Figure 6.2: quTool box

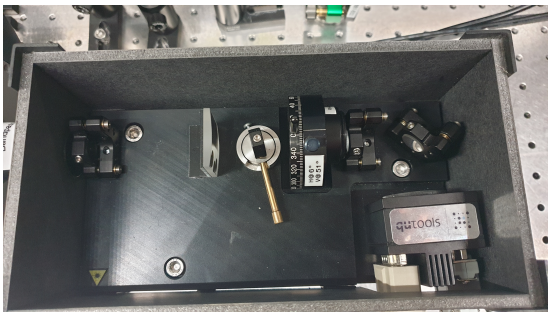

It is proven in literature that the coupling efficiency of the SPDC photons to a fiber is optimized by proper adjustment of the pump focus on the crystal. Hence, since the provided setup is devised for SPDC light collection from two fibers, the pump is focused through

a focusing lens placed at a focal length ahead of the crystal surface, as illustrated below in Fig**??**. The BBO lies within the Rayleigh range and thus the beam width is assumed constant w_o. It is also proven thought, that beam focusing alters the spatial profile of the SPDC light due to the spatial walk-off of the beam which introduces an asymmetry [**?**].

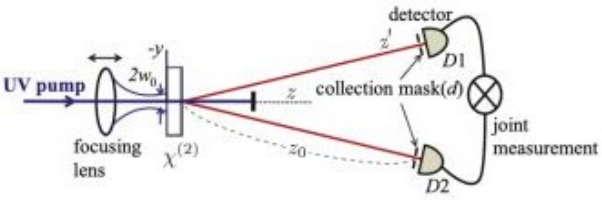

Figure 6.3: no threshold

For the systematic description of the SPDC produced with a focused pump, the biphoton quantum state must be calculated without using the transverse momentum conservation condition, because it comes from the assumption that the interaction area of the crystal is very wide, typically many orders wider than the scale of the wavelength, and that the pump intensity is nearly constant over this transverse area. Considering now focused pumping, the effective interaction area becomes relatively small on the order of several tens of μm usually, hence the pump intensity cannot be simply regarded as constant over the transverse region.

In Fig **??** are illustrated the numeric simulations of the spatial profile for a Type I non-collinear BBO under different pump focusing conditions.

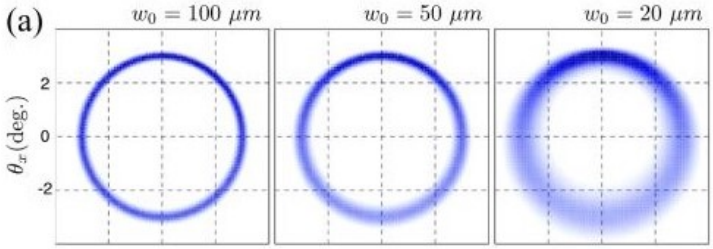

Figure 6.4: no threshold

It is clearly observed that the SPDC spatial profile becomes broader and asymmetric as the focusing increases. Specifically, the $-\theta_x$ direction is more broadened than the $+\theta_x$ direction, originating from the pump walk-off, where in negative uniaxial crystals the walk-off direction is the same as the broadening's. Finally, a similar observation is realized also in [**?**].

6.2 Black box quality measurement

For each set of measurements the box surface was covered with tape to ensure that the box lid is tightly attached to the box body, ensuring no stray light from the lab entering the setup. To verify the box quality, hereby is compared the histogram when the camera shutter is closed to when is open but the laser is not on.

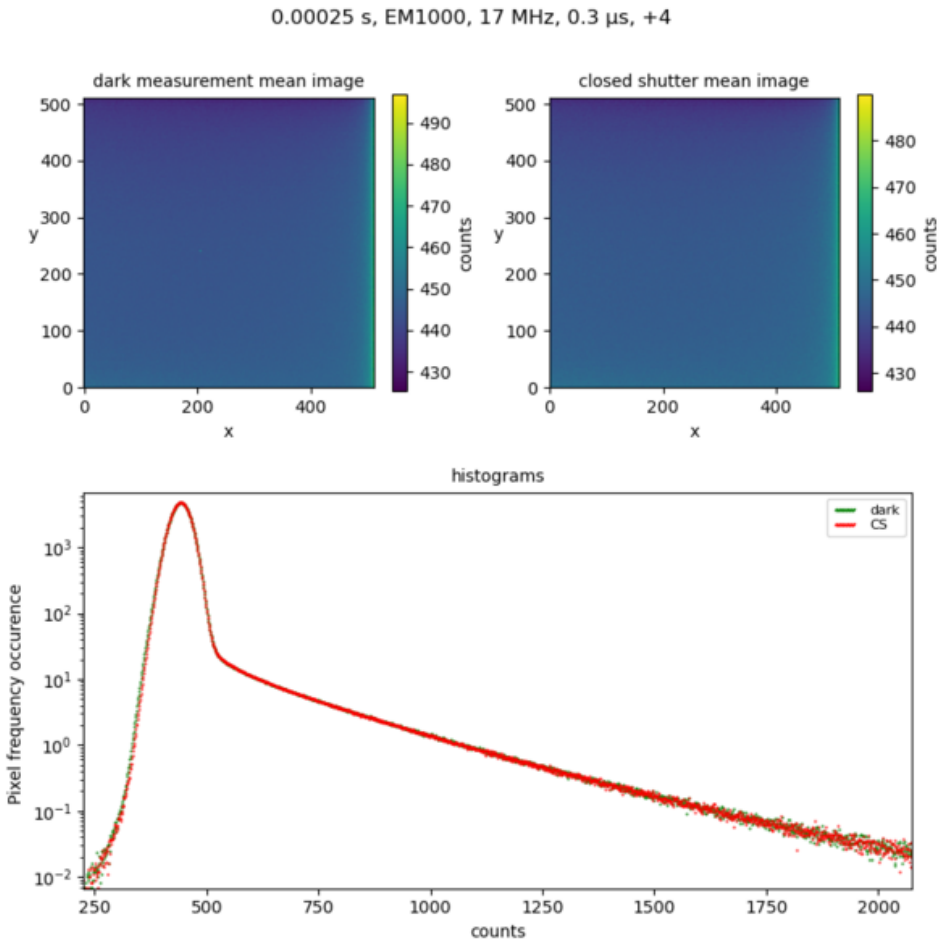

Figure 6.5: Comparison of open and closed shutter function in abscence of light, box sealed.

The slightly increased colorbar in the open shutter measurement is not due to stray light, but as observed in multiple frames due to cosmic rays detected in some of the frames within the measurement file that spike the counts in 1 to 5 pixels maximally per frame and the up to saturation usually counts, are absorbed in the averaging for the mean image.

6.3 Choosing the best mode of operation

The optimum mode of operation to acquire 1000 frames with the same exposure for each measurement file was found to be in Kinetic Series Mode, where the is no need for external triggering and the exposure time can be defined to the minimum possible the EMCCD provides, along with the liberty to choose the highest Readout rate and the fastest vertical shift simultaneously. Further, between scans, the Internal Keep Clean Cycle is performed when Frame Transfer is not applied, such that during the time between individual scans the Image and Storage areas are kept free of charge to ensure the data captured is a true reflection of the light that fell on it during the exposure period. Andor promises the best S/N when Frame Transfer is enabled, but I could not use it because the exposure must be larger than the time required to shift the image into the storage area =(image rows)·(vertical shift rate), hence for really small exposures and the whole sensor area active was impossible to use.

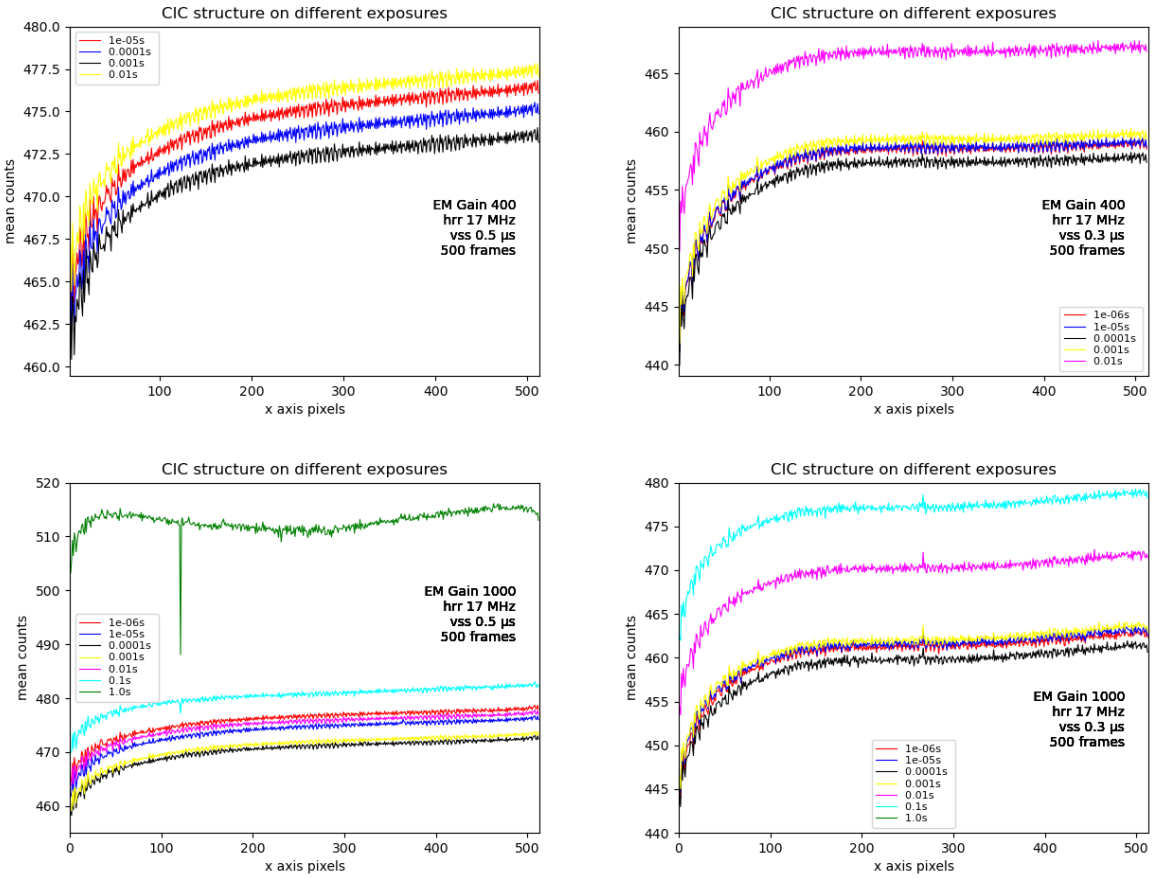

Figure 6.6: columns mean value of the whole sensor, over 500 frames acquired with closed shutter, for different exposure times. The 3.3 is a typo, in reality is 0.3vss!

As illustrated above, the choice of 0.3 vss compared to 0.5 is optimum, as the CIC events are significantly suppressed. For this vertical shift speed we must apply the maximum Vertical Clock Amplitude +4, to compensate for the charge transfer when the sensor is being 'overclocked' to eliminate possible charge smearing.

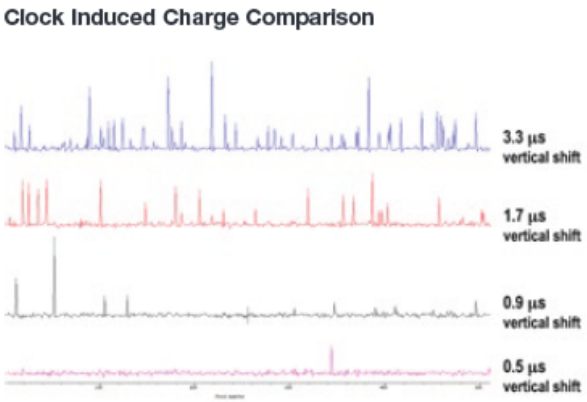

Figure 6.7: Dark images at EM 1000 at different vertical shift speeds for 29ms exposure with -85C cooling, measured by Andor.

The vertical stripes structure visible in the closed shutter images that have appeared during my analysis, are caused by the vertical CIC, which is not homogeneous across the frame, as illustrated clearly in Fig **??**.

6.4 Figure of merit kappa

The authors propose a device-independent figure of merit, called kappa, described as

$$\kappa = \frac{\left\langle \left(e_p^- - e_q^-\right)^2 \right\rangle}{\left\langle \left(e_p^- - \varepsilon_q^-\right)^2 \right\rangle} = \frac{\left\langle \left(n_p - n_q\right)^2 \right\rangle}{\left\langle \left(n_p - m_q\right)^2 \right\rangle} = 1 - \eta/2$$

where $\sigma^2\left(n_p - m_q\right)$ is the variance of the counts difference of opposite pixel pairs in the same frame, divided by the difference variance of the same pair but the opposite pixel value is taken from the next frame. The variance of the same frame pair suffers from the shot noise since the raw data considered here are not thresholded and the presence of noise is constant in every frame. The measurements were performed under EM 1000 as stated in the paper, probably because they aimed to span the full exposure time range under the same camera setting. Otherwise if someone is not operating the camera in photon counting mode, the SNR does not benefit from the extra EM application, on the contrary in high fluxes the EM well capacity saturates before the pixel well depth does.

In the low exposures we expect the downconverted photon to be lost within the multiple CIC and stray light from the laser. With increasing exposure time, the downconverted signal will be dominant compared to the CIC, hence distinguishable and definitely emerging from the readout out noise floor. Along the whole exposure range, the signal is shot-noise limited not only due to its nature but also due to the excess noise factor. To obtain $k < 1$, demands $\sigma^2(n_q - n_p) < \sigma^2(n_q - m_p)$. Due to the Poissonian statistics in each frame, the statistics between frames will be Poissonian as well.

The average is done over 1000 frames for my data, while theirs 100. These opposite pixel pair locations of the downconverted ring, are denoted by $p = (x, y)$ and $q = (-x, -y)$, with x and y discrete pixel numbers with origins in the center of the ring.

As we can observe in gallery **??** for 2x2 data where the contrast is better compared to no binning, the background values are lower than those on the ring, meaning that the variance between frames on the background is large than the one on the same frame at background, whilst on the ring the sequensial frame variance is smaller than the one in the same frame.

A figure of merit promising that dividing the variance of the difference between opposite frames with variance of the same pair but with the one pixel in the next frame, would yelp the ring area correlated below noise.

I found the opposite behaviour compared to the one described in their paper. In low exposure times where the frames do no exhibit the same constant illumination in the exact same positions, we obtain a good contrast where the background is the appear as correlated light and i assume due to the fact that it gives a constant output when its difference is measured throughout all the exposure times. On large exposures, every photon is correlated to every other randomly resulting in blurry output with zero contrast.

The center of choice was calculated according to the figure of merit kappa, at large exposures where i could observe a pattern. If had explored first the correlation measure scheme, then I would plots r' for different center choices and would have chosen the one for which the correlation value would be the smaller.

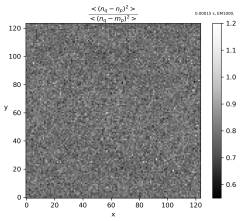

(a) 0.00015s, K, 2x2 bin

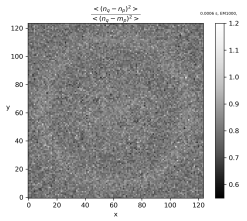

(b) 0.0006s, K, 2x2 bin

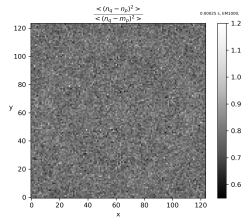

(c) 0.00025s, K, 2x2 bin

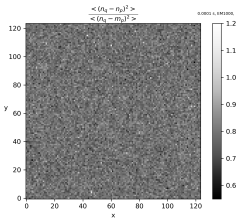

(d) 0.0001s, K, 2x2 bin

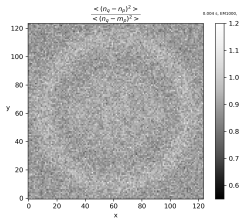

(e) 0.004s, K, 2x2 bin

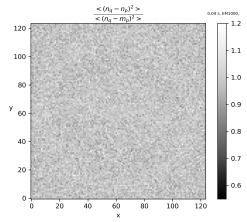

(f) 0.04s, K, 2x2 bin

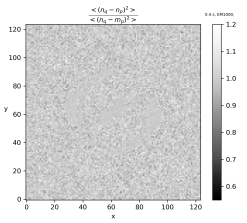

(g) 0.4s, K, 2x2 bin

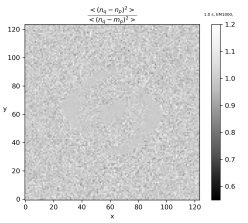

(h) 1s, K, 2x2 bin

I tried further binning 4x4 where the contrast is improved, irrelevantly of the increase of the coherence area here, the representation of the collected light on the image after binning, on the ring area is drastically amplified compared to the lowe background. In the case of 8x8 any difference in the signal of the neighboring pixels is just lost completely after grouping.

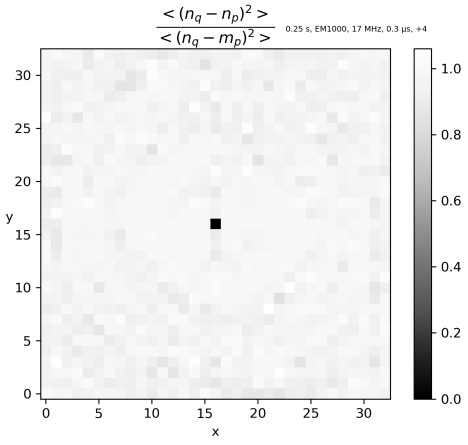

(a) 0.25s, kappa on 8x8 binned data

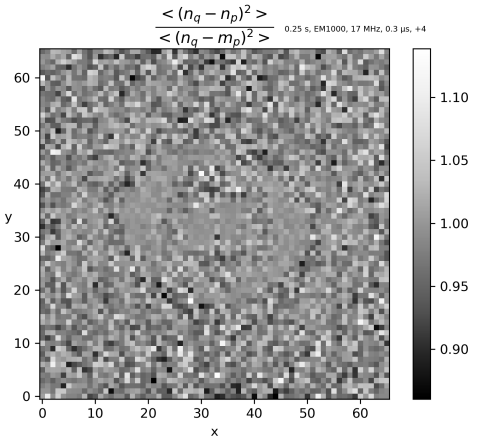

(b) 0.25s, kappa on 4x4 binned data

6.4.1 Origin for cropping choice

To calculte the center of origin for cropping, i plotted multiple offsets from the original choice with all 4 directions possible simultaneously shifts and chose the cases were the shape counts discrepancy while overlapping the rings was minimum, at maximum exposure time (Fig **??**) where the colorbar scale is large for better resolution. I provide a lower exposure also for comparison in Fig **??**.

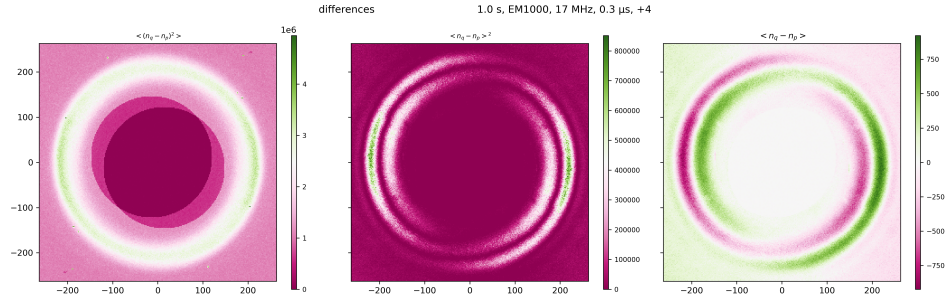

Figure 6.10: 1s, no binning, center choice

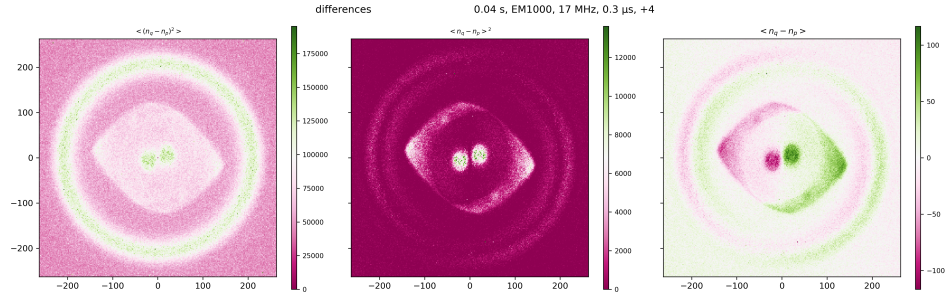

Figure 6.11: 0.4s, no binning, center choice

The safest choice was made after the 4x4 binning where the ring geometry is more clear on its outer diameter, by choosing a range of 5 pixels until the crop boarder from the 'whitest part ' ring outer part at the 4 sensor middles.

Before I concluded to this method, I was curious trying out the procedure proposed in the paper 'Massively Parallel Coincidence Counting of High-Dimensional Entangled States, 2018', where they obtain 10^6 frames, choose a pixel on the sensor that its opposite is desired to be found, and for each individual frame they multiply all the pixels with the one chosen. Eventually a some contribution in the opposite correlation area will arise, corresponding to possible correlate spatially photons.

I managed to sum only 8000 frames of the full frame picture, then cropped trying as symmetrically as possible around the ring. Due to the low frame number and the absence of lens for the necessary fourier transform, it seems like I measured a random mixture of the position and momentum plane, hence I would not consider these pictures as accurate representations of the correlation diameter.

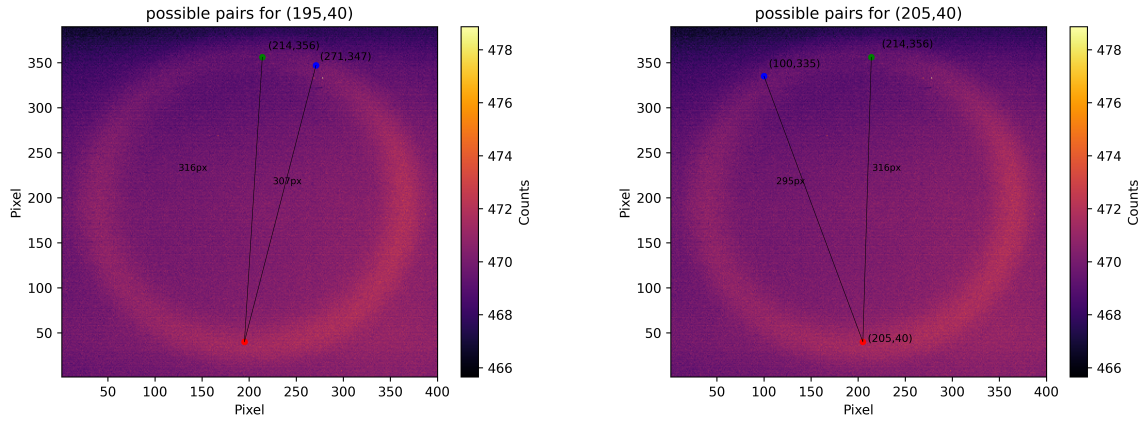

Figure 6.12: Chosen pixel marked in red, possible pairs in green and blue.

Further, to find a rough estimate of the annulus center i obtained the max value of each row and column of the 2D stack.

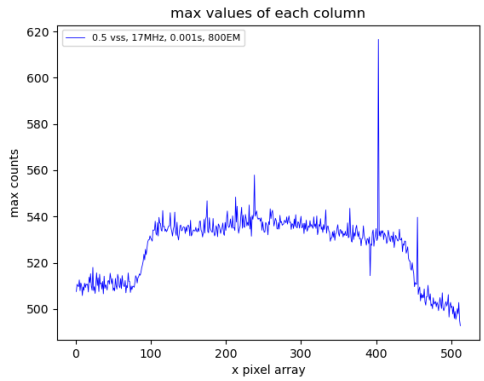

(a) maximum value of each column along x axis.

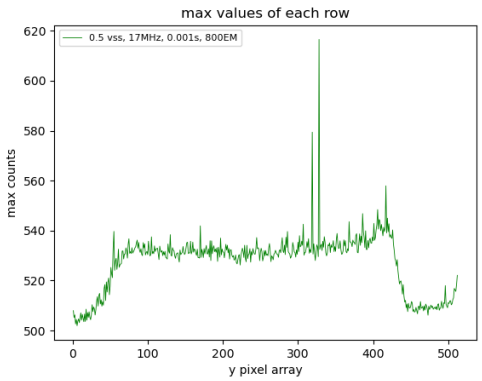

(b) maximum value of each row along y axis.

The spikes in the counts represent the two small bright areas in the top right side of the ring. They appears to be 'black pixels', because they are always much less brighter then the rest of the sensor as i have noticed, where it is not obvious in closed shutter measurements because everything is in the noise floor anyway or, where they can't exhibit lower values.

Before optimizing the setup with a Fourier lense, I tried estimating the center of the ring by approximating it with a on its clear boarders where the diagonals would reveal the center, as illustrated below.

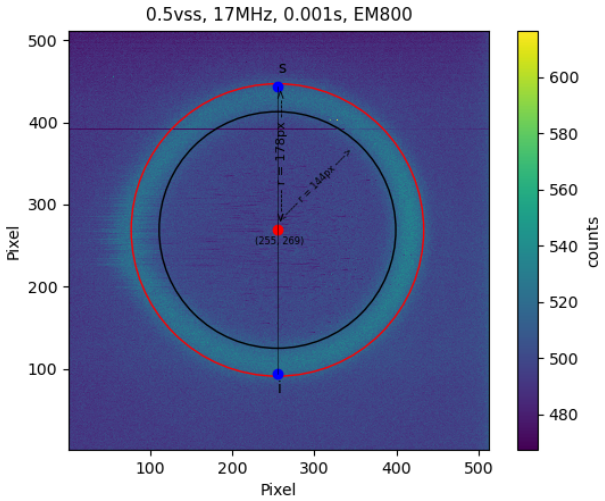

Figure 6.14: annulus outer limits for $x_1 = 54$,$x_2 = 425$,$y_1 = 101$,$y_2 = 450$

After imposing the circles it was very clear that I should choose the 0.3vss to restrain the vertical smearing that even further distorting the ring shape, accidentally in the same direction that the pump walk-off does too, as described in the setup.

6.5 Photon Counting Mode sub-shot noise correlations

Following the procedure described in [**?**], I calculated the correlation measure for three different low exposure times, where i also encountered the case of binning my data 2x2 and 4x4, where in the first case the resolution would equal the coherence area of my source and the latter, twice, as normally shall be and is applied by the authors. In the first analysis, because I binned the data after thresholding them, i had the choise to continue treating each photon number within a sector as 1 or using its true value during summing.

The concept of using binary data is to account for 1 or 0, when binning after imposing threshold and continue treating the data as 0 or 1 we loose all the necessary information. A better approach that i haven implement, would be after thresholding and binning, to consider the superpixel as 1 or 0, judging by if it has or not any non zero counts.

Instead of restricting the analysis to 180 sectors, I calculated the correlations for 90 , 120 , 180 and finally 360 sectors. for each measurement frame, i create the respective amount of sectors by a transformation of the pixel coordinated to radial, hence asymmetric opposite sectors result in some cases. The sectors radius is 8 pixels maximum, accordingly to binning.

The three lowest exposure times that fulfilled the condition of average flux per pixel $\mu << 1$ are the 0.010s, 0.015s and 0.025s.

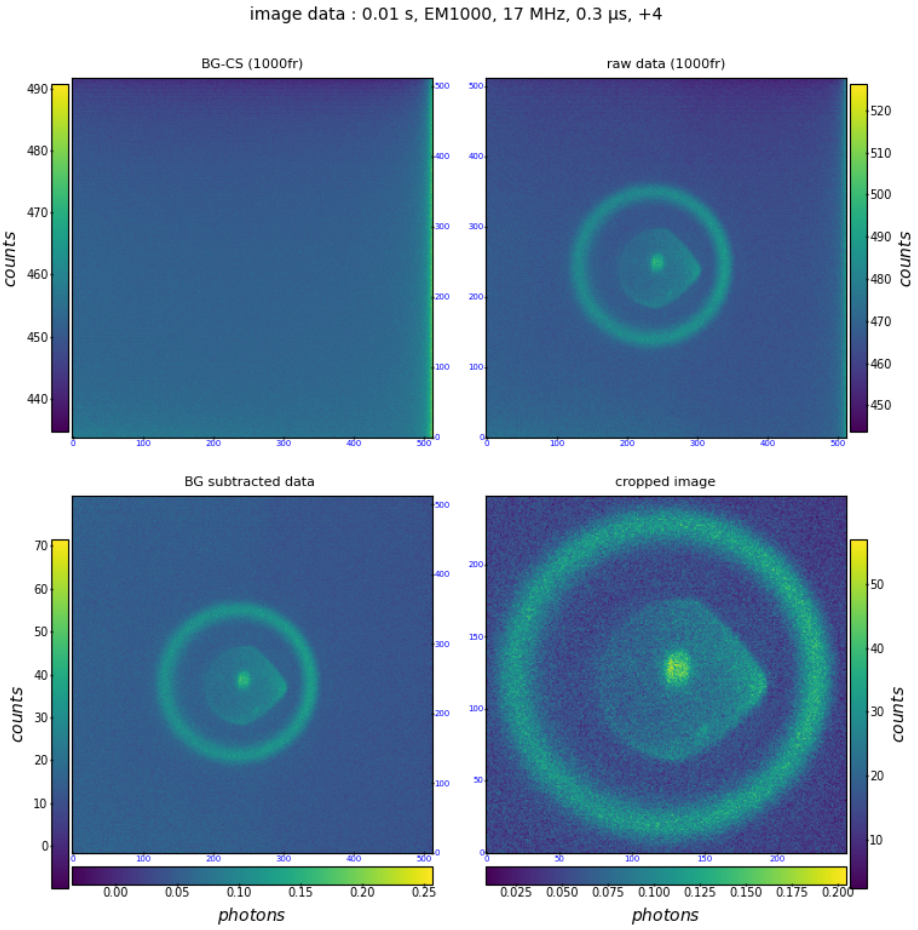

Figure 6.15: a)Mean image of 1000 frames with background data when shutter is closed. b)Mean image of 1000 frames raw data with laser on. c)Mean image of background subtracted raw data. d)Mean image of cropped background subtracted raw data.

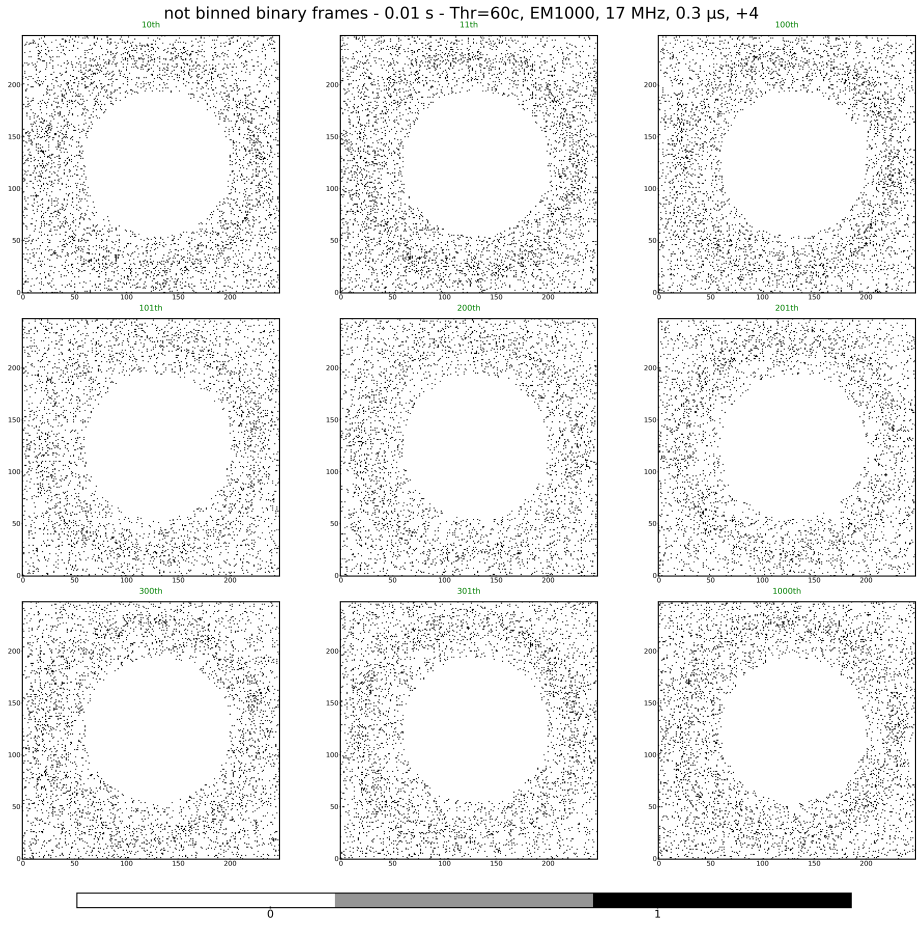

Figure 6.16: 4x4 binned frames, 0.10s

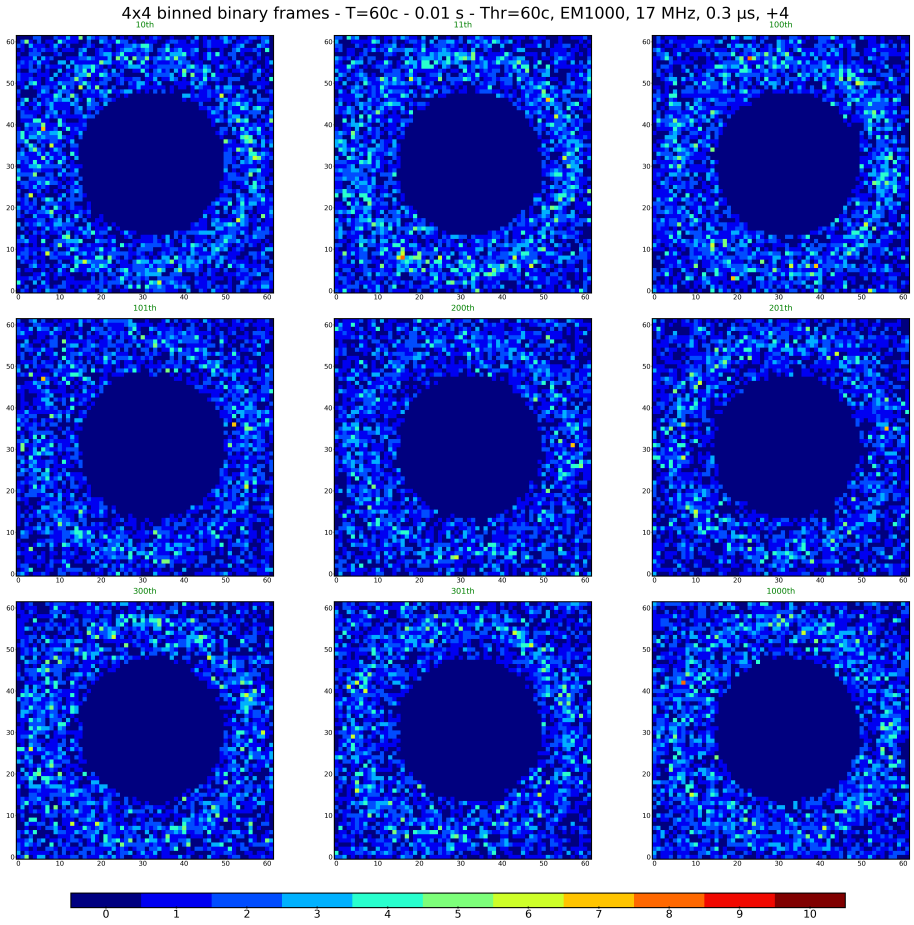

Figure 6.17: thresholded 4x4 binned frames, 0.10s

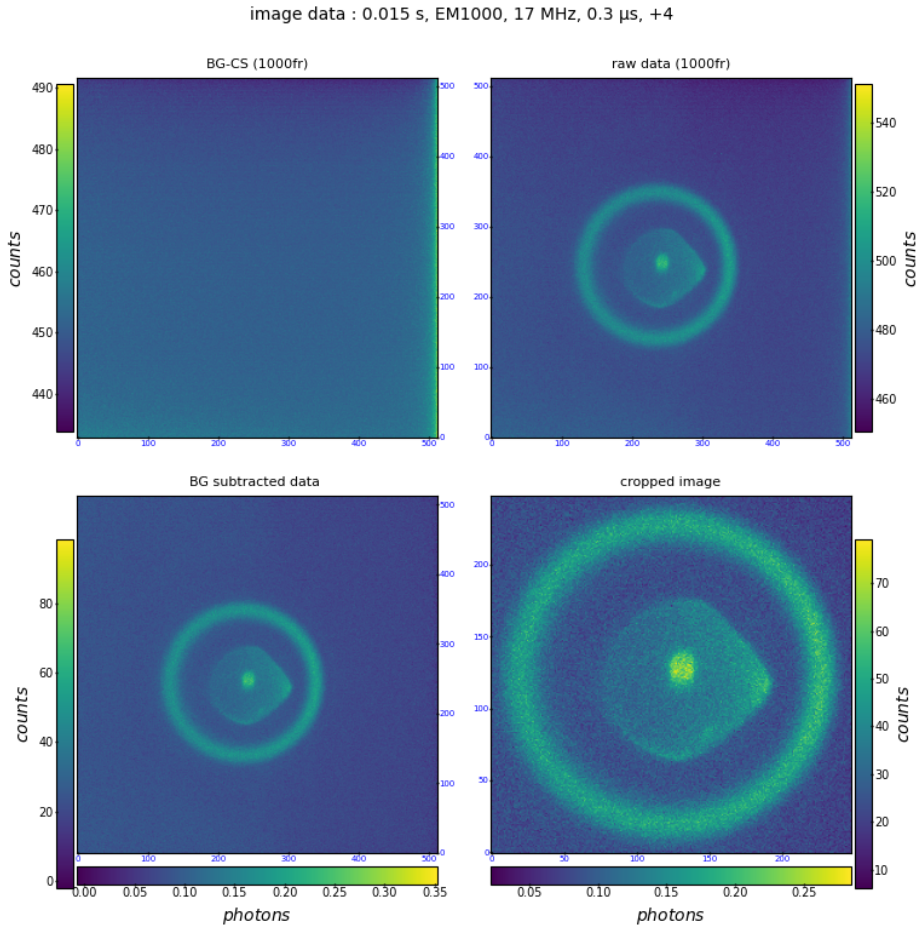

Figure 6.18: a)Mean image of 1000 frames with background data when shutter is closed. b)Mean image of 1000 frames raw data with laser on. c)Mean image of background subtracted raw data. d)Mean image of cropped background subtracted raw data.

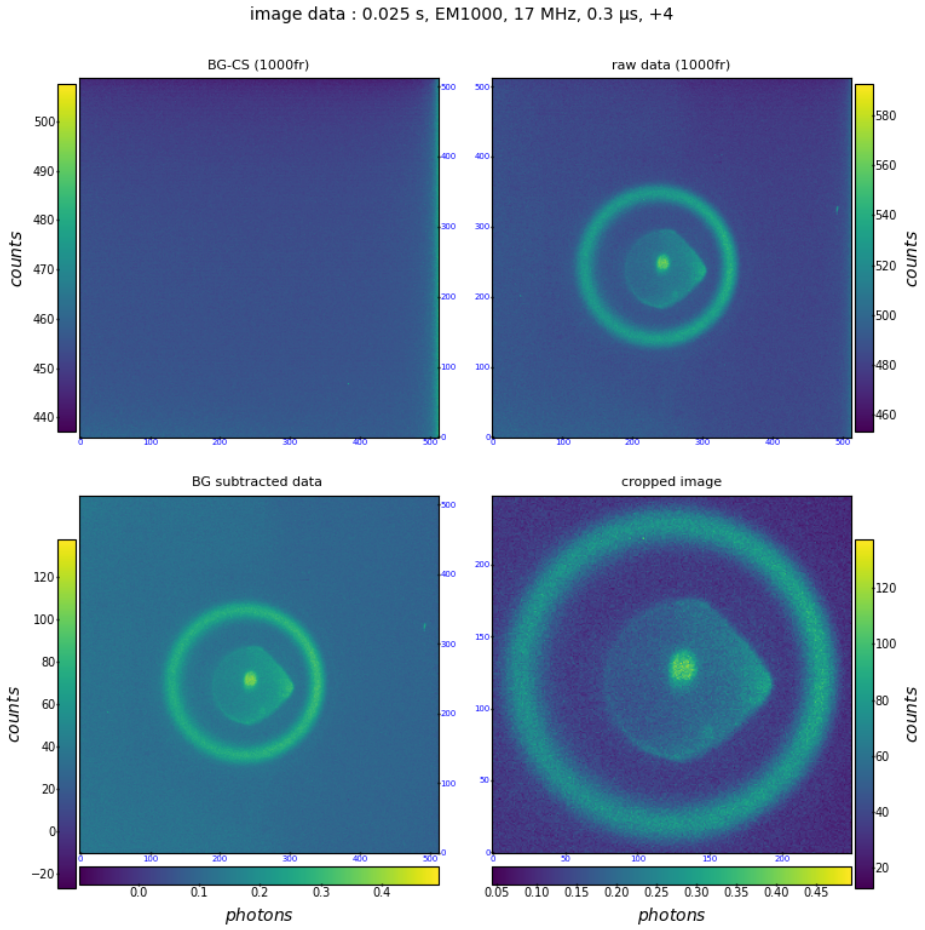

Figure 6.19: a)Mean image of 1000 frames with background data when shutter is closed. b)Mean image of 1000 frames raw data with laser on. c)Mean image of background subtracted raw data. d)Mean image of cropped background subtracted raw data.

6.5.1 Summation as numbers

These collective plots describe the behaviour of the correlation measure, according to the binning and the number of sectors defined, three for the three different low exposure times.

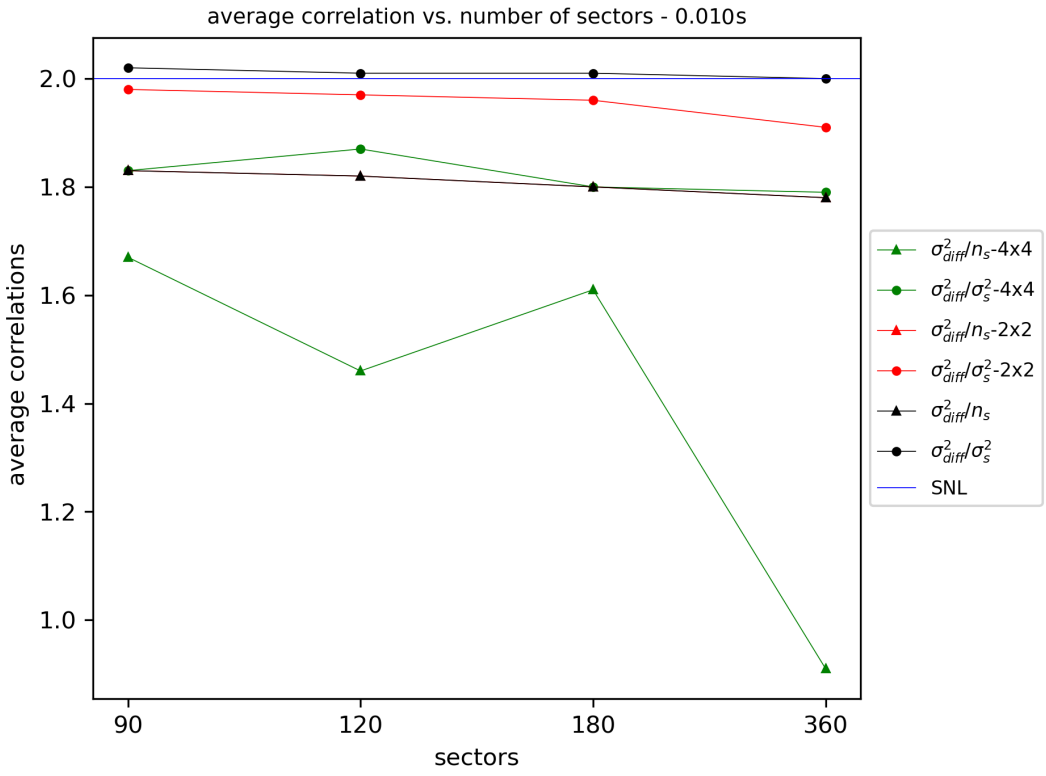

Figure 6.20: real photon number accounted

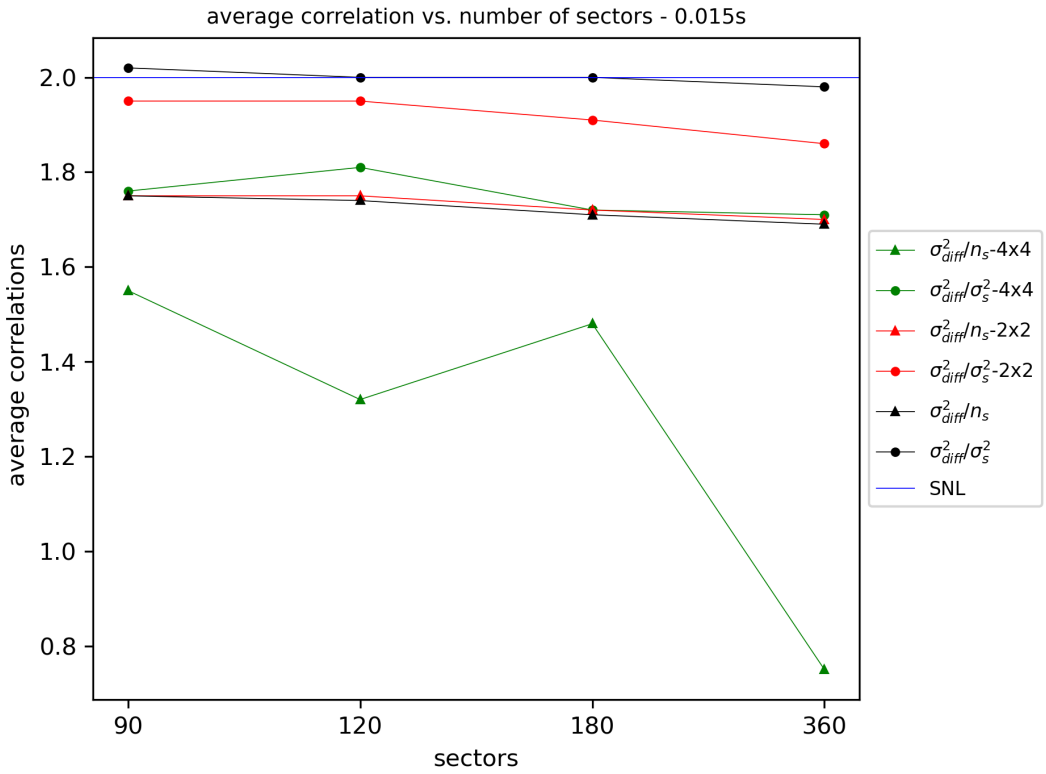

Figure 6.21: real photon number accounted

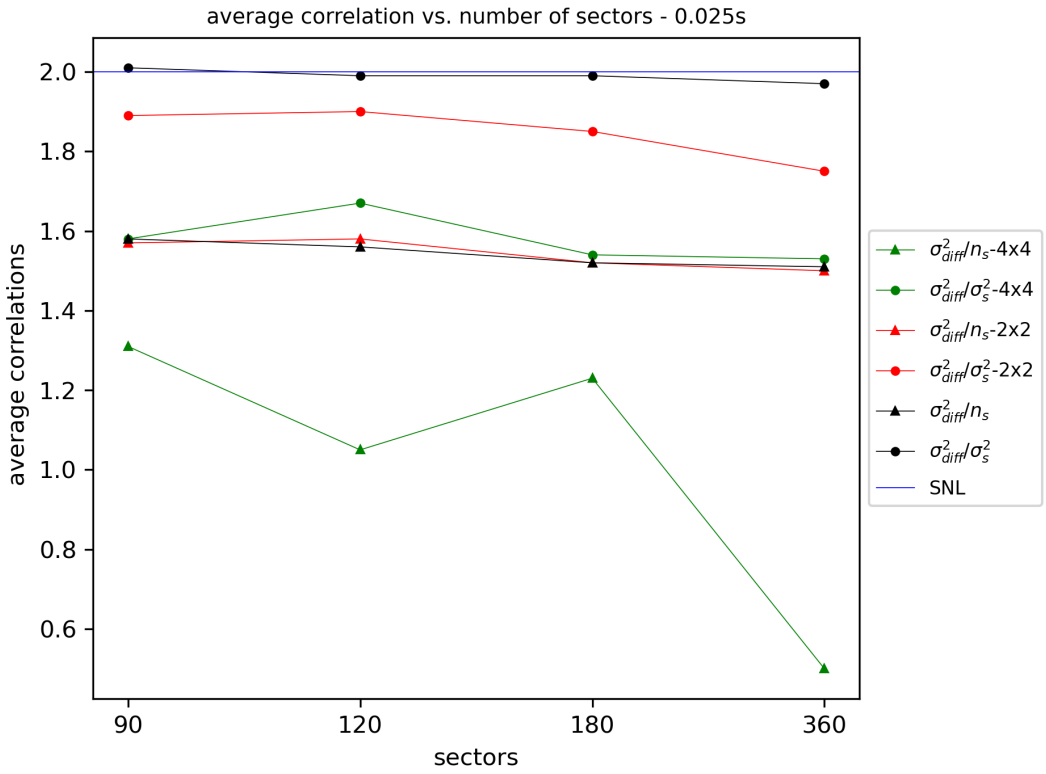

Figure 6.22: real photon number accounted

The only case with correlation defined well above (2σ) without binning is at 360 sectors, excluding the smallest exposure. This verifies that my experimental calculations on the coherence area of the pump, where 17mm lens would be required to reduce it below the pixel area ($16\mu m$), while with the 25.4mm lens we are at 1.7 pixels uncertainty area. For this reason, we observe decrease with 2x2 binnin, but not as efficient as with 4x4.

I must stress here, we cannot bin at maximum and expect near zero corellation values, binning size comes with the cost of its center uncertainty determination. When we have none binned data, the uncertainty of the origin definition can be defined up to a pixel. When assuming a superpixel, the uncertainty in position is defined by the superpixel's half size, hence in 8x8 binning will be 4 pixels, which affects drastically the measured correlations. From multiple literature has been mentioned that for their setups the ideal binning choice was either to double or equalize the detection area, compared to their coherence area.

We observe an overall decrease of r,r' with binning for all the exposures and sectors, but the 120 sectors that exhibits a peculiarity. The r binned cases there increase for the two larger exposures, while for r' increase. It seems that the photon variance there is lower and the average photons higher.

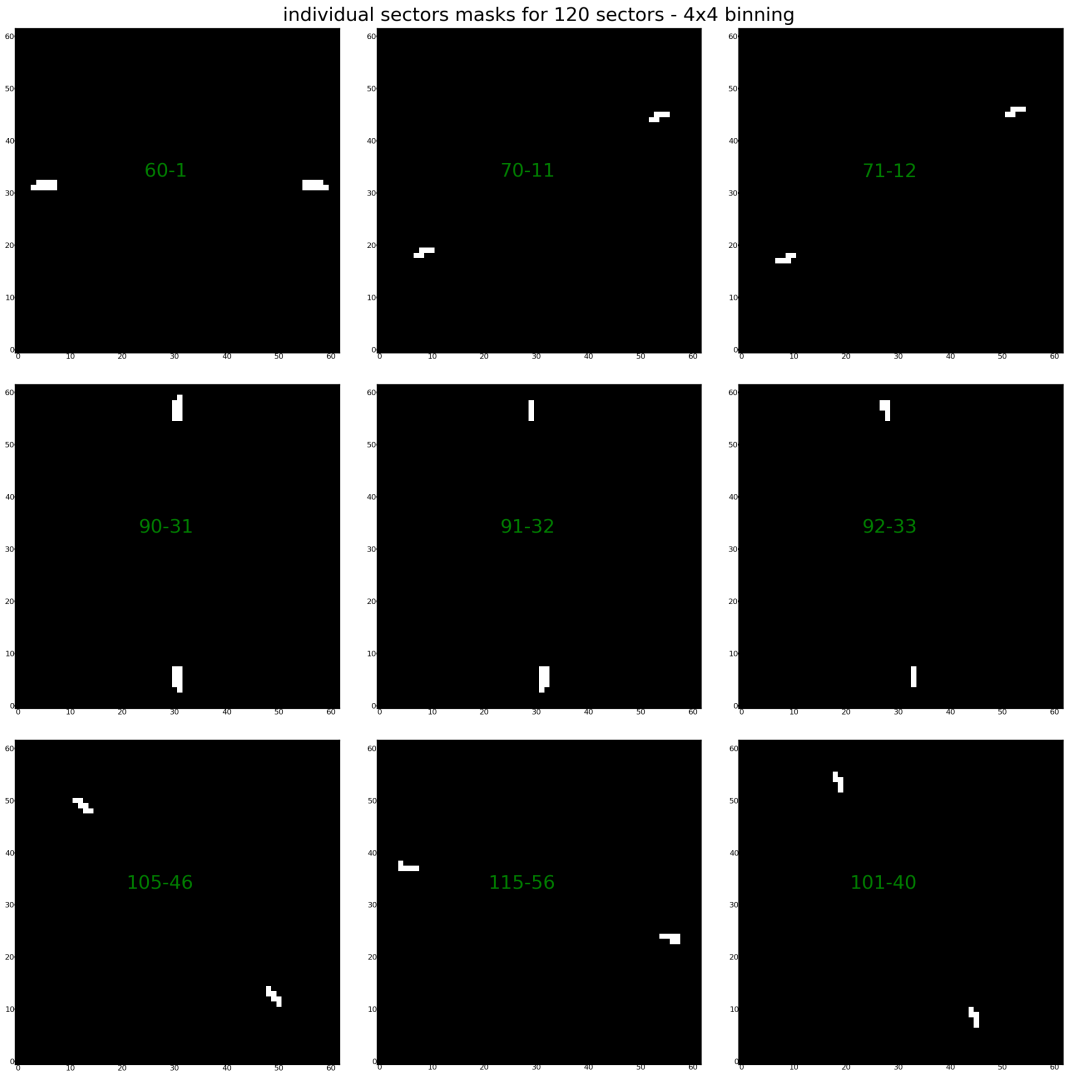

Figure 6.23: opposite sector mask pairs definition for 4x4 binned data, 120 sectors.

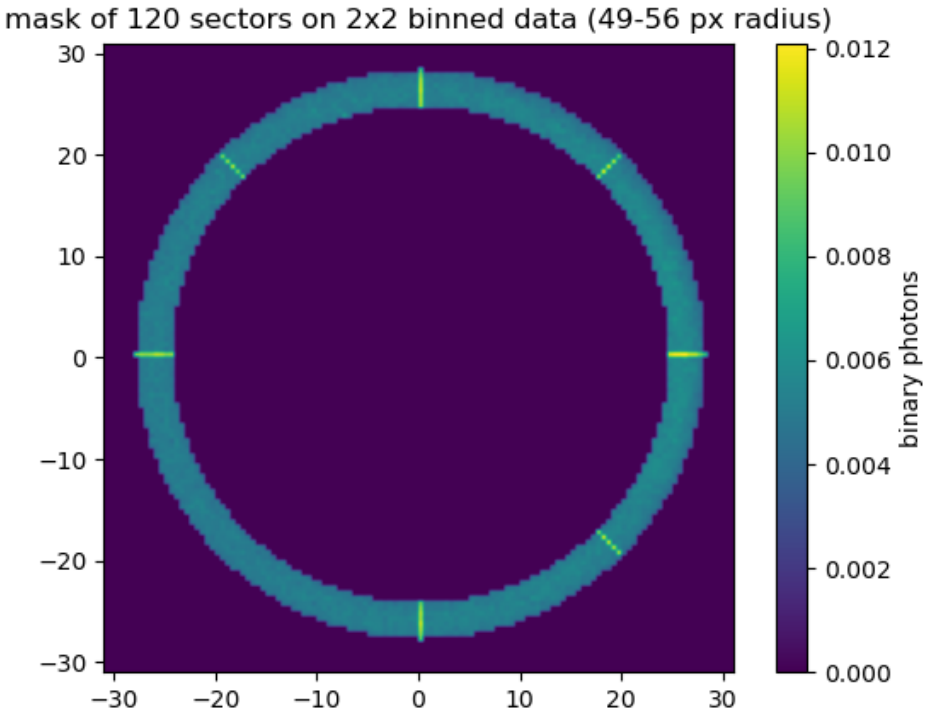

Figure 6.24: overall mask for 4x4 binned data, 120 sectors.

below follow 2 sequential frames show the distribution of binary photons in them

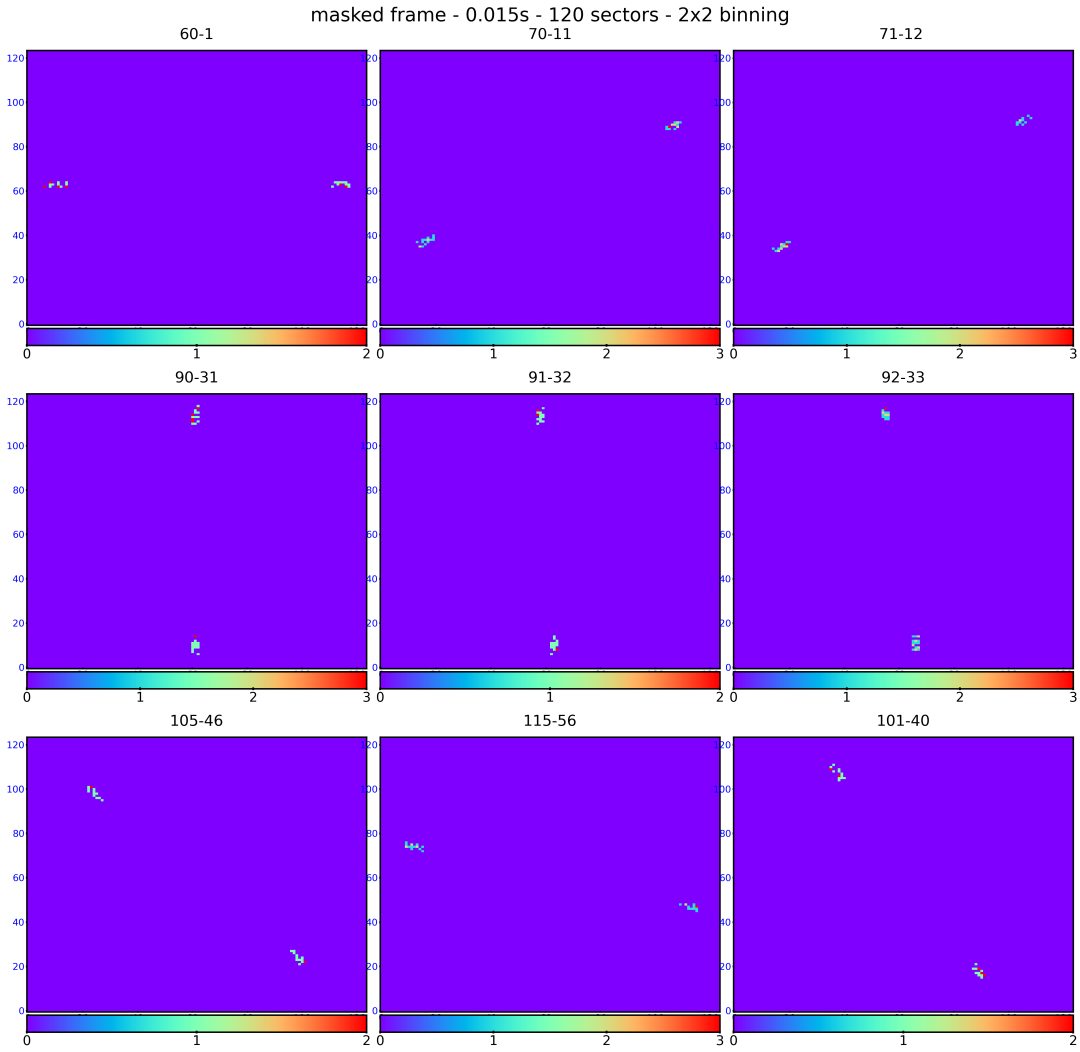

Figure 6.25: overall mask for 4x4 binned data, 120 sectors.

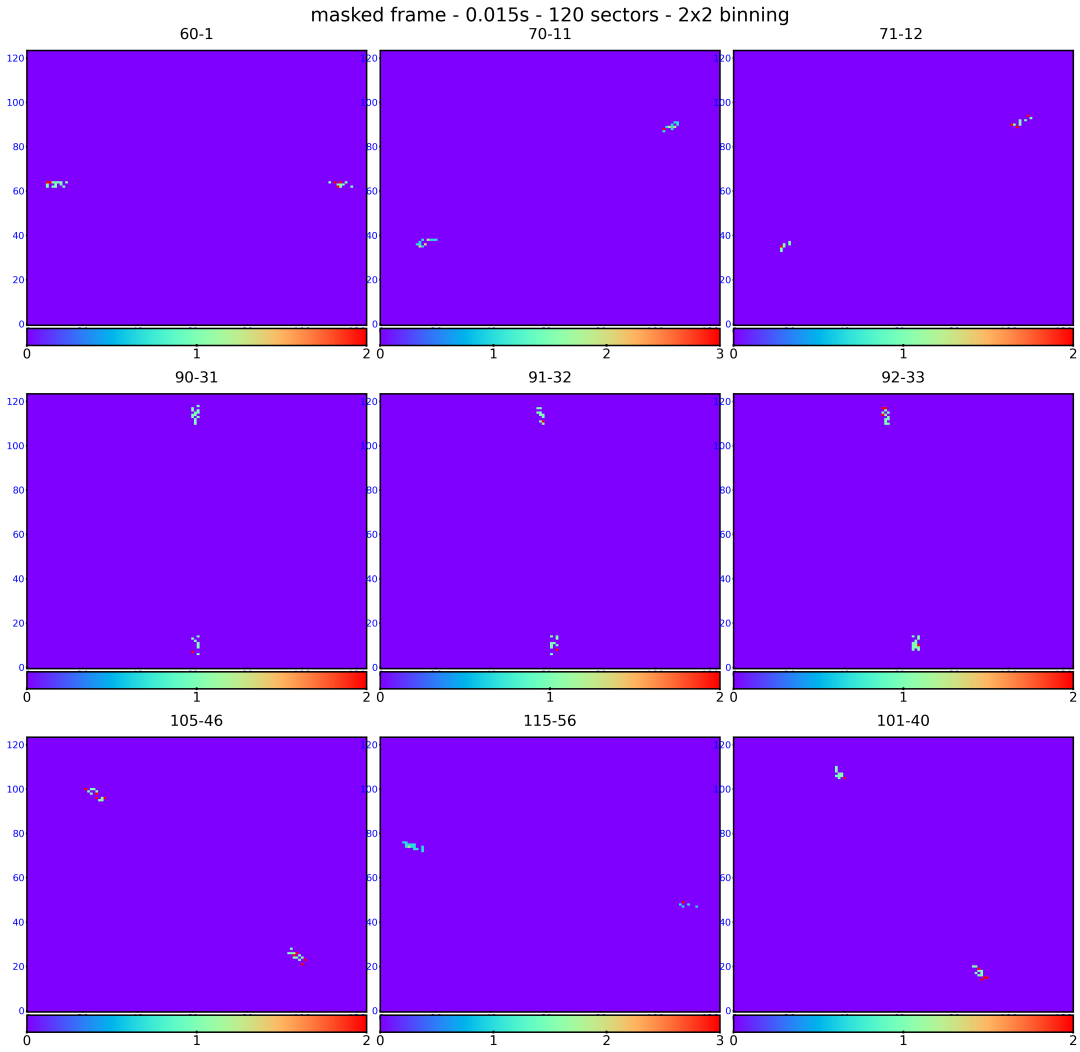

Figure 6.26: overall mask for 4x4 binned data, 120 sectors.

In the last two mask, the total amount of photons contained within a sector seems equal to its opposite, thus indeed the photon variance is further reduced.

The sets of images arranged bellow containing what is also illustrated in the first collective plots, is in order to check the large values of the standard deviation, while in the collective plots only the averaging error is plotted which is the standard deviation divided by the square root of the amount of frames.

In Fig **??** one can observe the origin of the high standard deviation, which stems from the laser power fluctuations, increasing/decreasing respectively the amount of produced photon but also the background. Normally if the optical path is properly optimized, laser fluctuations shall not affect the results that drastically.

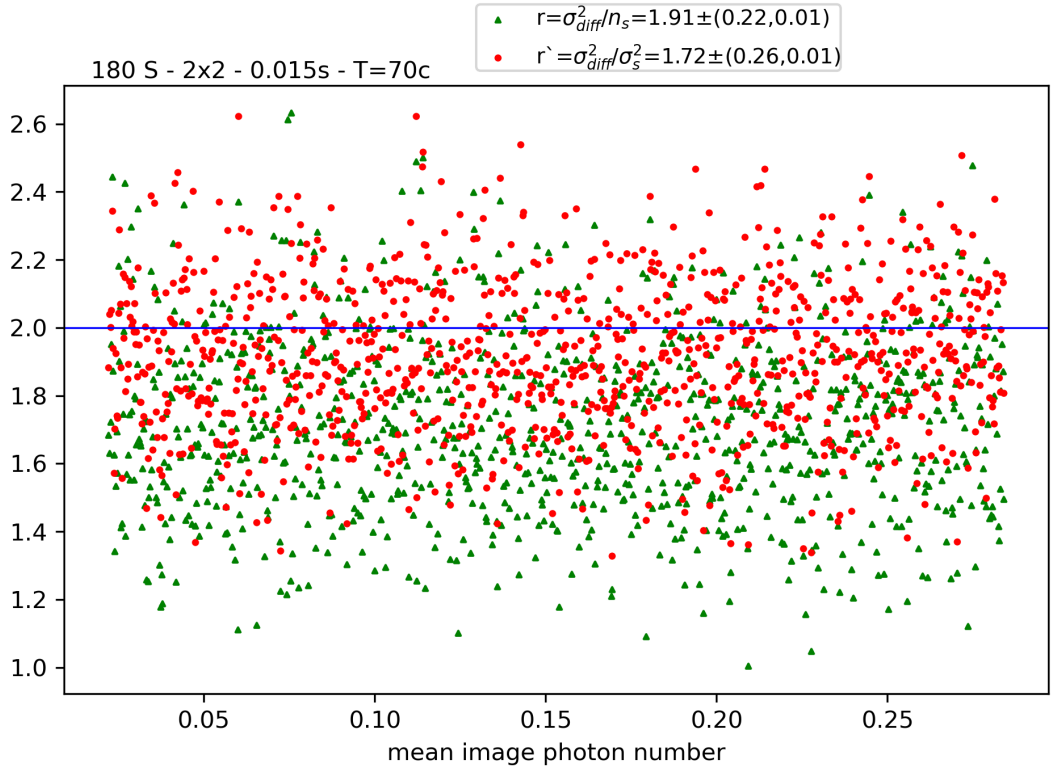

Figure 6.27: correlation measures for 2x2 binned data, 180 sectors.(RED and GREEN swapped in the legend!)

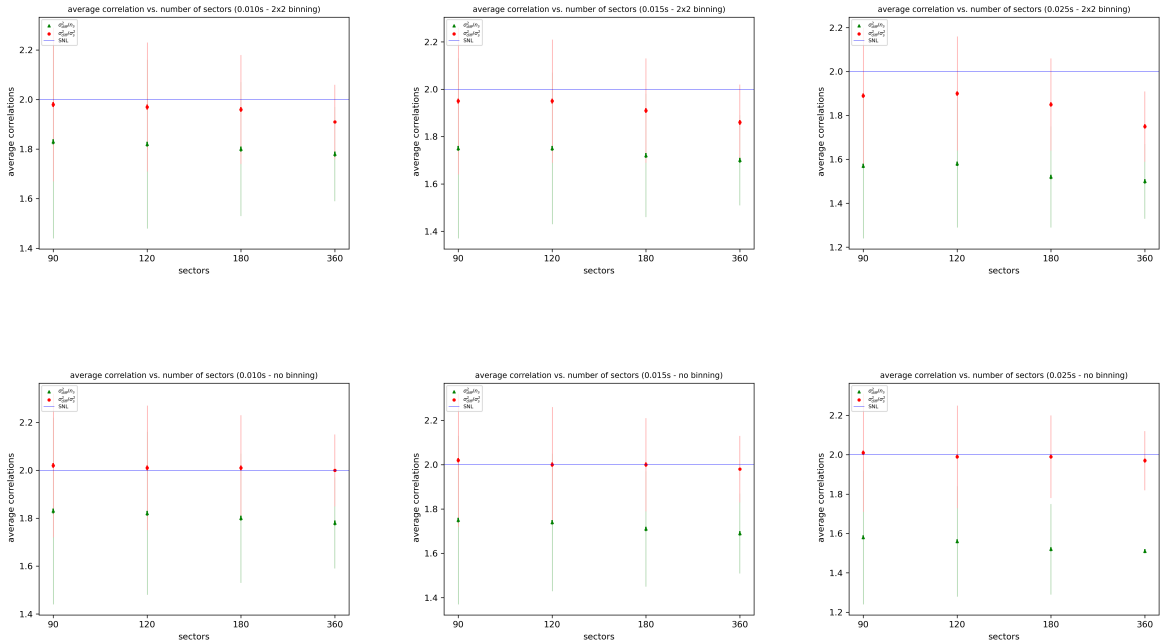

To conclude here based on all the above plots, the case of 2x2 for our setup would yeld the same result as if we had an uncertainty area equal or slightly smaller to the pixel, the case of 4x4 would mean uncertainty half of the detection area , as wished in most cases cases for good resolution. The minimum correlation measurement that can be achieved is defined by the overall quantum efficiency . The quTool thich filter reduces it drastically, yet we dont have an adamant measure of it but is suggested at $0.3 - 0.6$, the premium filter is of the order 90% and sensor quantum efficiency at 810nm at 75%, reducing to an overal 0.45%.

Hence a minimum value of 0.95 can be accepted for r and r'. Now concerning the case of 360 sectors at 4x4 binning, because the sector number is too small and thus the amount of photons contained inside them too, it is equivalent to realizing the case of the Noise Reduction Factor, where below 1 is translated as sub-shot noise measuremt with minimum limit at 0.45%

6.5.2 Summation as non-zeros

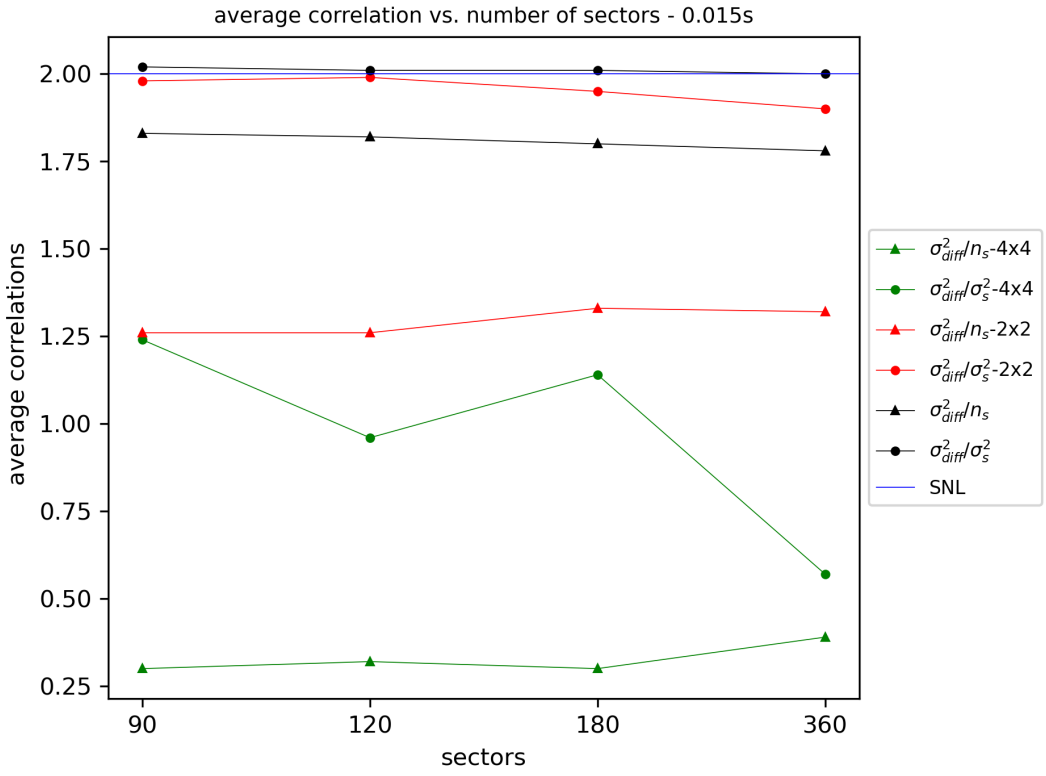

Figure 6.30: every non-zero photon =1

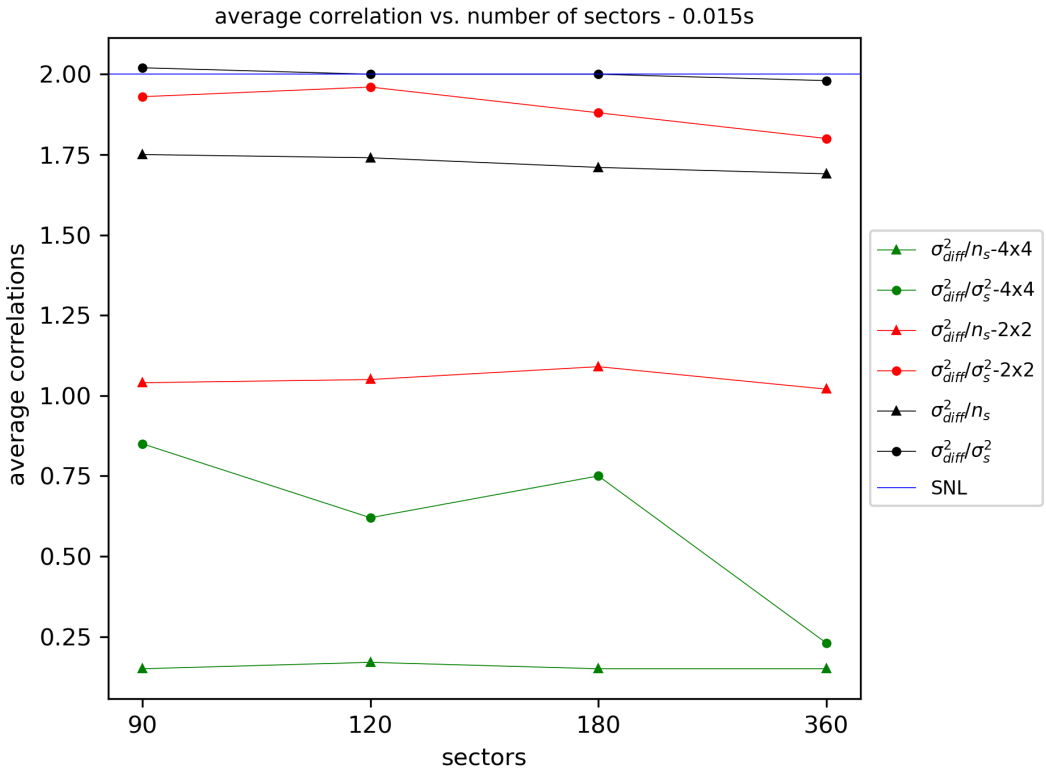

Figure 6.31: every non-zero photon =1

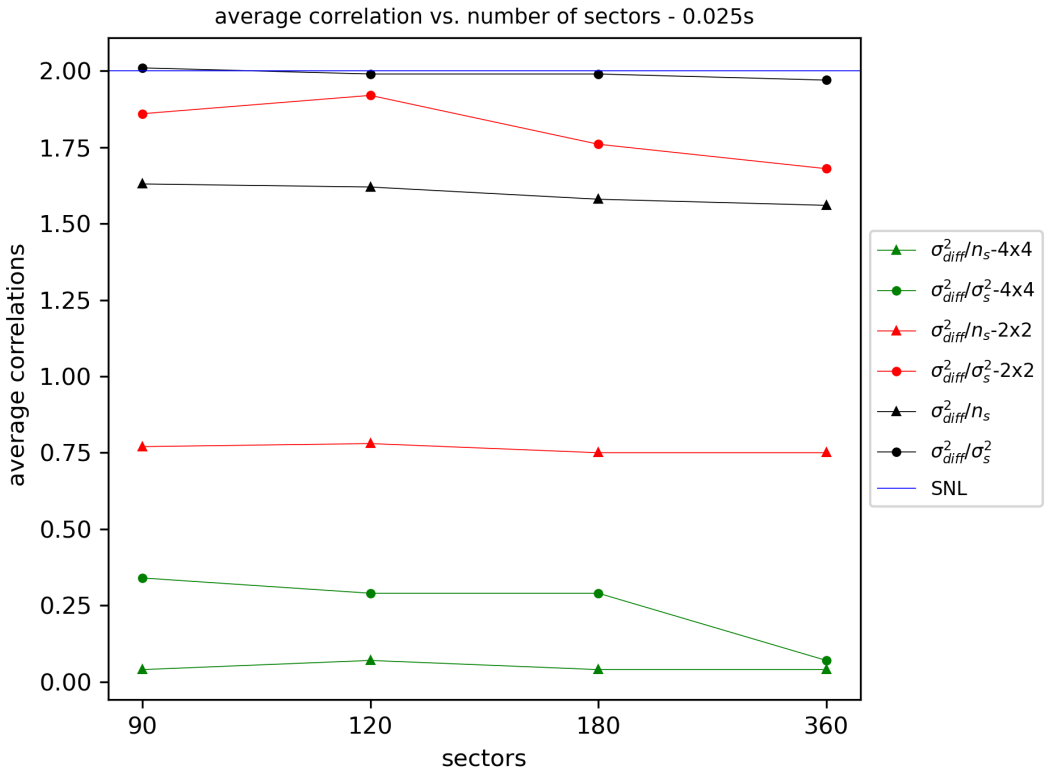

Figure 6.32: every non-zero photon =1

The values for no binning on data, are as expected equal to the case we dont treat the numbers as non-zero. Here now the 4x4 case for division by variance has the same behaviour as 4x4 case in the same exposure time but for dividion with photon number. Since r is always lower than r'. somehow similarly here is 2x2 affected, having the same behaviour as in the other plot but now it starts from a value divided by 2 compared to the same exposure time.

In general along larger exposure time the values drop, but the photon variance division of the 2x2 case is not affected. This scheme can be considered as thresholding the binary data, where the critical information on the number of photons is lost and the correlations are underestimated. We could easily say that it gives values not allowed by the quantum efficiency minimum.

I must mention here that the the 0.025s exposure for non-zero treatment, has been treated with a threshold at 85counts instead of 58, by mistake, hence they are not expected to reveal the true correlation measure.

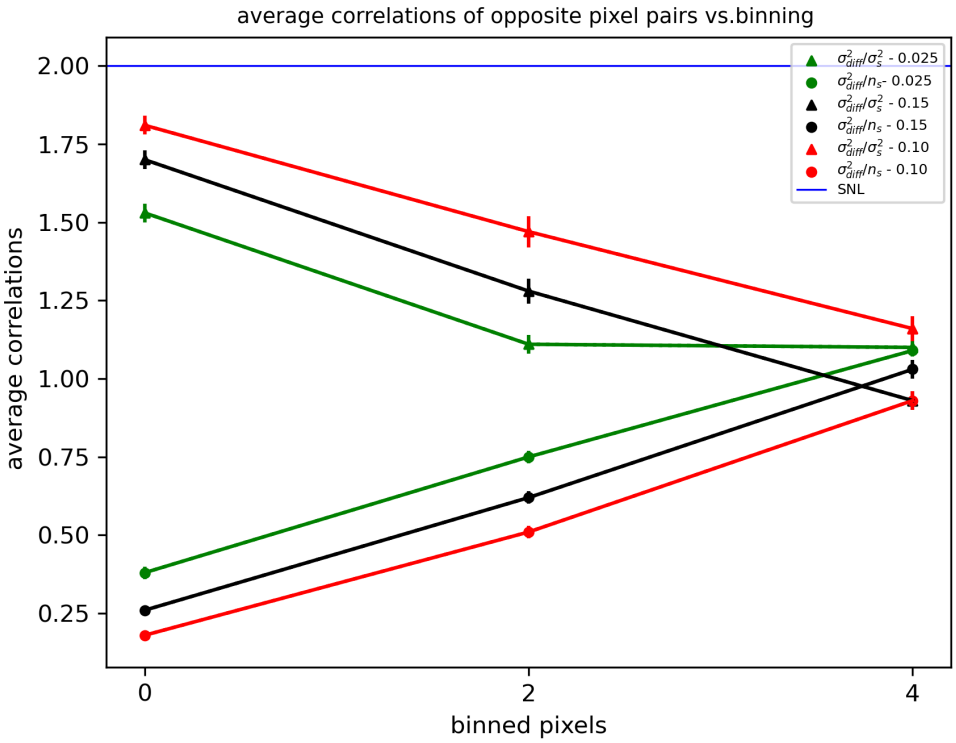

Figure 6.33: sector=pixel, every non-zero photon =1

In Fig **??** is illustrated the collective plot, where every pixel is treated as a sector. For each frame, a copy is created that is rotated by 180^o and deduced by the original, verifying that we obtain the difference variance between only antidiametric pairs along the sensor.

The respective plot for the case where the photons were treatred with their real value is not illustated here, but even though its absence, I must mention that for no binning the values were laying around 1.7 and 1.9, for 2x2 and 4x4 binning in the range of 3 to 5 irrespectively the exposure time. Hence in both configurations r' was increasing but in this one r is decreasing

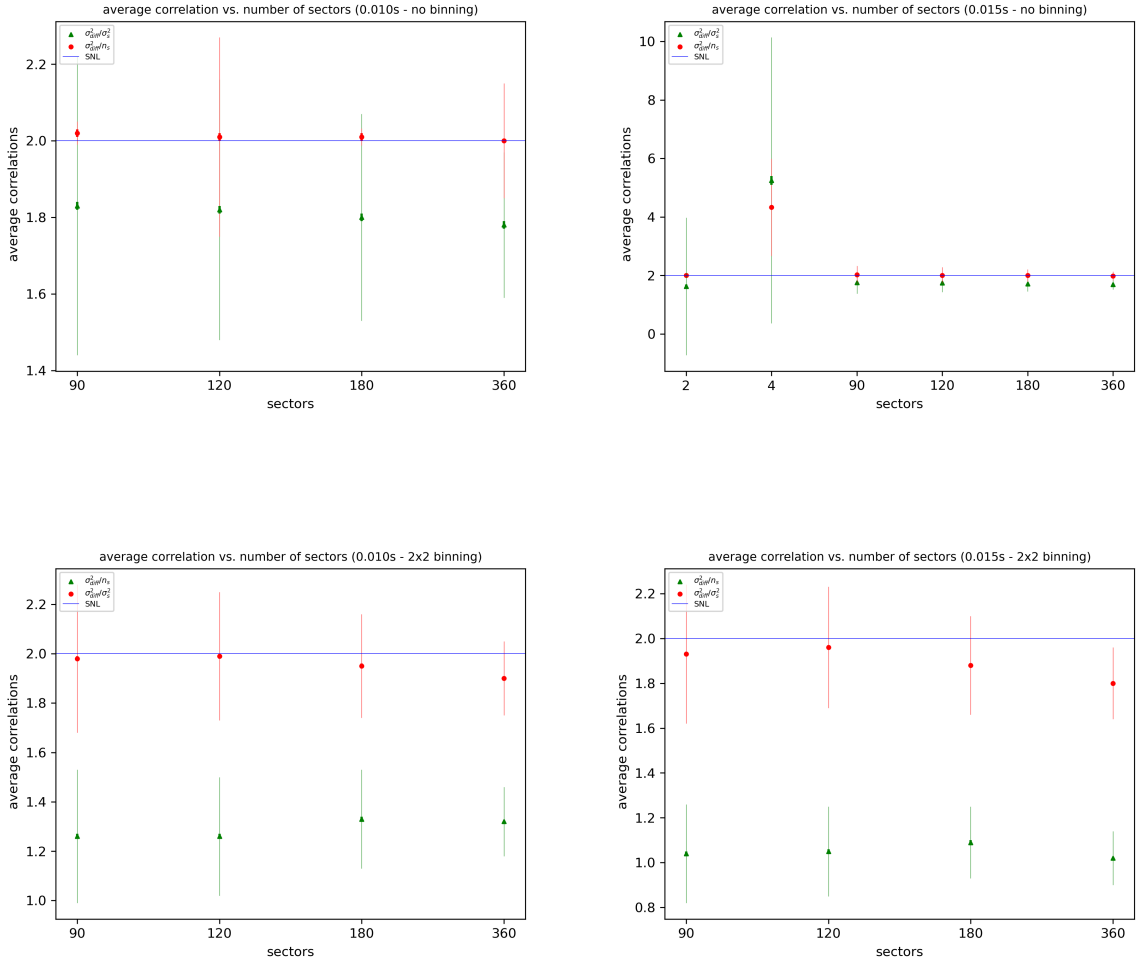

Here I chose to show a collective plot where i had included the calculation of 2 and 4 sectors. To obtain the results for 2 sectors, I did not divide as defined in the equations because it would yeld nan values, it was just to play around with the data. What is obtained for the 4 sectors though is quite interesting, the exhibit way above the SNL values and in my opinion is because the binned light will exhibit the smaller photon number variance . The 4 sections of the ring are unsimilar in counts between them but but locally, overall this counts discrepancy is lost.

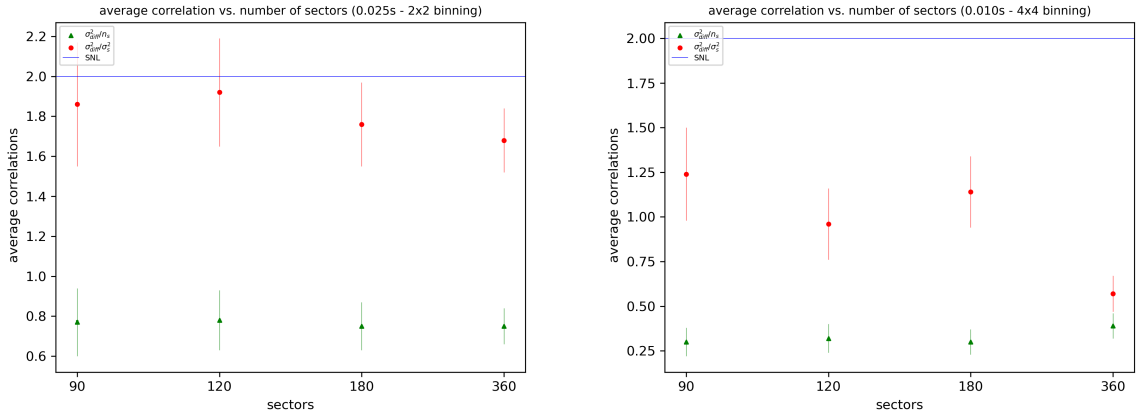

It makes absolute sense to have better results for higher exposure time, because the lower the exposure

the higher the noise. Assume the extreme example that i would have noise and only 1 actual photon pair, then everything would be correlated to everything and i would have wrong numbers. the more pairs i have the more correlations of true pairs are registered , so i have better results indeed.

The reason in opposite pairs at 4x4 binning that are overestimated is that i have really low variance of the photon number, so i divide something with something really small and i get large number that is overestimated. One way to treat that, would be to assume that the superpixel has 0 value or 1 if any of the contained in the binning have a non zero number. Dont forget that the expression in the photon counting paper is given only for binary data, this is also the reason that i kept treating them as binary, but not in the appropriate way (saying that the whole superpixel equals 1 if just one of the pixels have value 1). This is further enhanced by the fact that the opposite pixel pair noise reduction is giving great results, because after thresholding at 4x4, isnide one superpixel i had from 0 to 4 photons but I was diving with A+B that could be from 1 to 8, while in the upper case I divide with the mean number coming from all the sector/pixel averaging is very small.

The plots in this section correspond to data that belong to opposite pixel pairs within an angular mask of 8 pixels wide, along with the calculation the Noise Reduction factor according to Eq **??** .

The noise reduction scheme for anti-correlated photons detection relies on the ability to detect large number of anti-correlated events, where the objective is to maximise the number of joint detections of photon-pairs, while minimising the number of detected single events. The downconverted photon-pairs constitute the pair events, whereas single events can be detector's dark events (dark electrons, CIC), partially detected photon-pairs due to optical or detector's losses, or uncorrelated photon events due to spurious background illumination (fluorescence, ambient light, or longer wavelength present in the UV pump).[**?**]

Optical losses and spurious background illumination can be mitigated by careful adjustment and alignment of the optical components, where unfortunately for this setup it was not possible due to the limited space between the camera entrance and the filter mounted on the quTools box, thus the Fourier lens with respect to the optical path towards the detector is not perfectly aligned (a small tilt might be present because it is not mounted and the body of the 25mm lens is quite large). One thing that might optimize the setup further, would be tilting the interference filter mounted in the camera entrance, to maximise the joint-detection of downconverted pairs at degeneracy, with respect to the filter's transmission window. The reason that the highest EM gain is used is to maximize the photons detection and minimize the lost joint events.

It can be clearly seen that anti-correlated light exhibits noise below SNL, while the uncorrelated light above, indicating the noise originating from the laser flair and the CIC. The CIC for these low exposure time, is lower than the actual photon rate, so the main noise originates from the fact that we could not perform a proper background subtraction where the laser is on but the crystal not inside the optical path, in order to eliminate the laser light background. The fluctuations of r from frame to frame is attributed to the laser power fluctuations and the confirmed presence of noise (CIC and laser flair)

Concerning the results of r between these three different exposures: for larger exposure it is expected to produce and detect more correlated events, whereas the CIC events are constant in probability(within this slightly different time window) and the laser flair is a constant background increasing linearly with exposure, but never more than the downconverted events. The better r values of 0.015 s exposure compared to 0.010 is due to the amount of downconverted photons being larger than those of CIC. The largest exposure of 0.025s gives the lowest values in all cases, this could be due to the overthresholding, where even though the readout noise and the CIC are totally excluded, yet the chance of having 2 or more photons impinging on 1 pixel is getting higher. Assuming 2 photons in the latter case impinging simultaneously in 1 pixel, could be either scattered light in combination with 1 downconverted photon, or 2 downconverted photons from two different pairs, or 2 random photons. The first case would give a photon in the opposite pixel position as well, ideally, accompanied or not by stray light and we would have a correlated event measured. In the second case, again we would expect 2 photons ideally in the opposite pixel, where again we have registered a correlation event. Finally in the latter case, it is the same as having 1 random photon impinging somewhere in the sensor and being accounted as a single event. In conclusion, increasing the

chance of double photon detection in our scheme, within reasonable limits, due to the anticorrelation of the photon, does not severely deteriorate r compared to as having single detections. Of course if we were investigating different phenomena where the spatial entanglement was absent, the double detection probably would probably deteriorate such a threshold scheme.

no binning - 0.010s

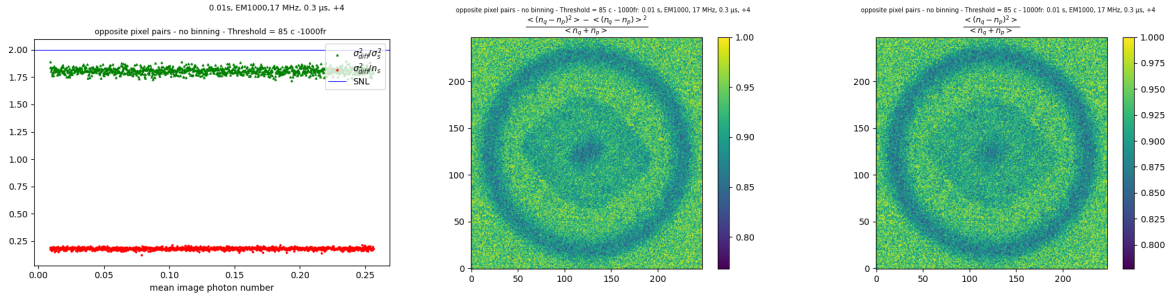

Figure 6.37: 0.010s, no binning, Thr=60 counts.

no binning - 0.015

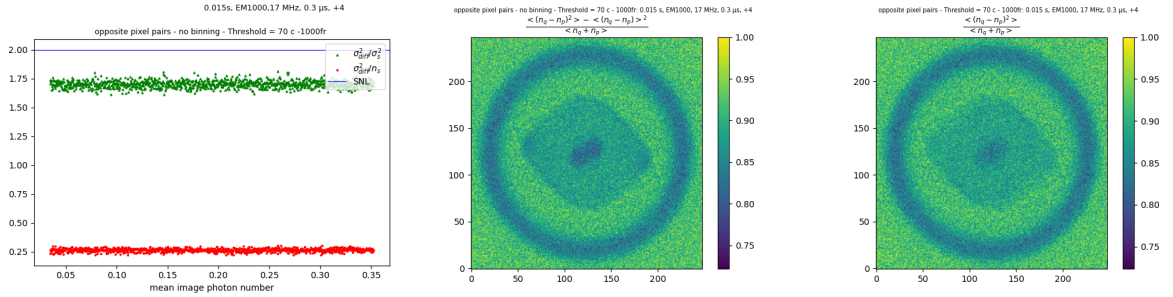

Figure 6.38: 0.015s, no binning, Thr=70 counts.

no binning - 0.025

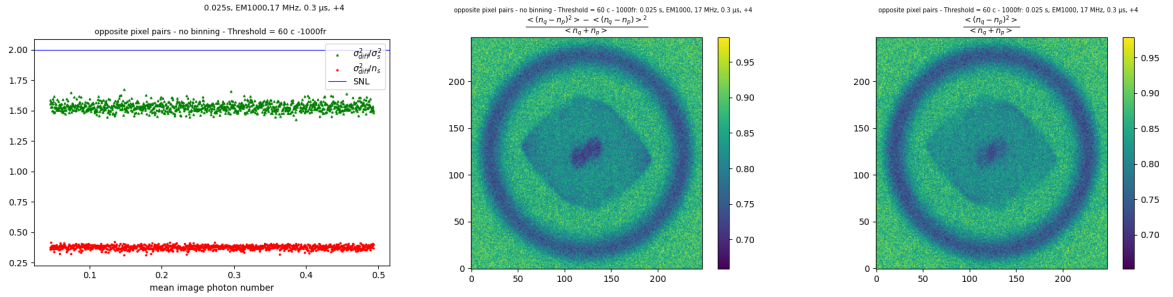

Figure 6.39: 0.025s, no binning, Thr=70 counts.

2x2 binning - 0.010

The previous plots of r where compared with those where the variance suffers its full expression. Here the figure of merit Kappa is calculated for the thresholded data this time, to see if any difference is observed, but still as illustrated we have a blury noisy result.

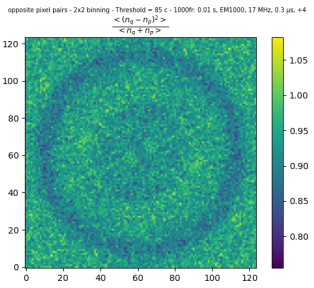

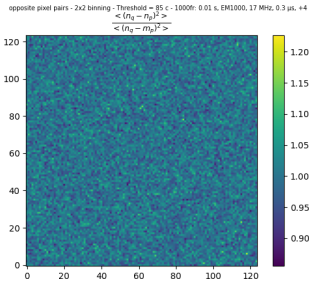

2x2 binning - 0.015

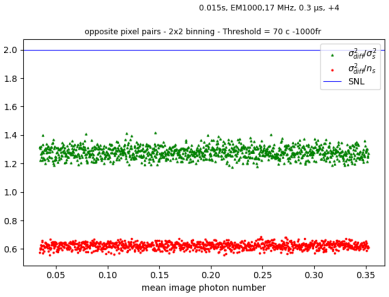

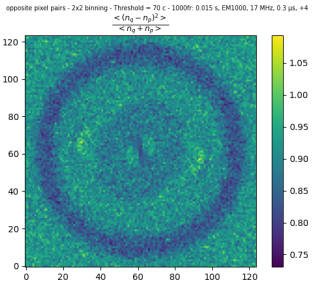

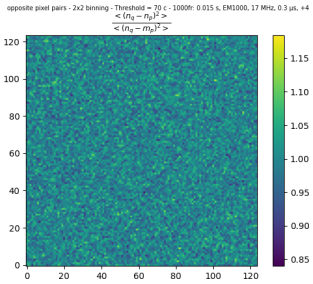

2x2 binning - 0.025

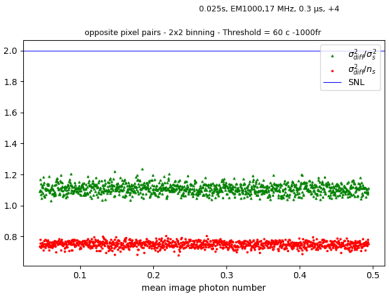

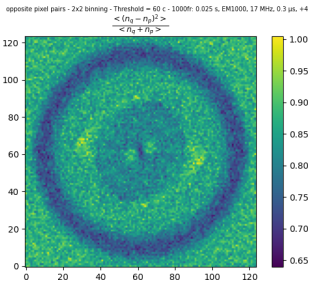

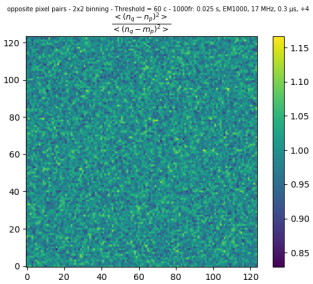

4x4 binning - 0.010

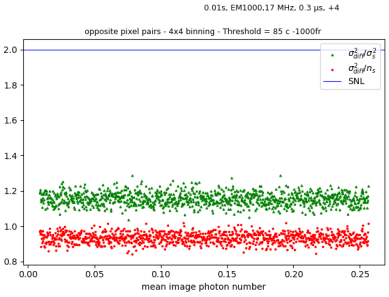

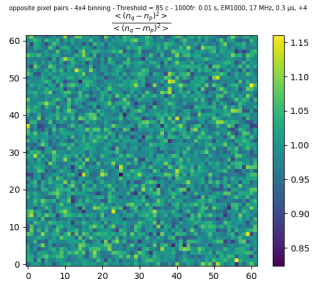

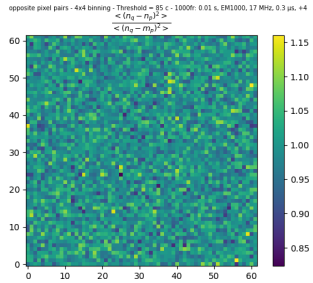

4x4 binning - 0.015

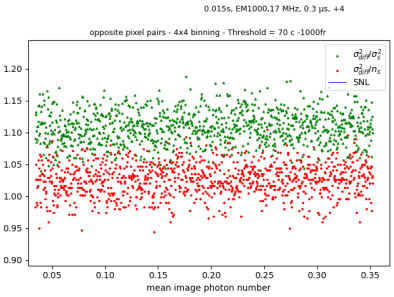

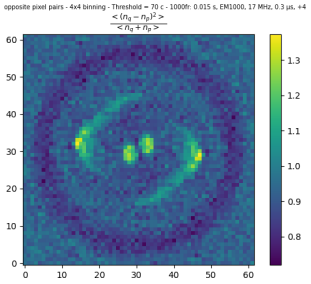

4x4 binning - 0.025

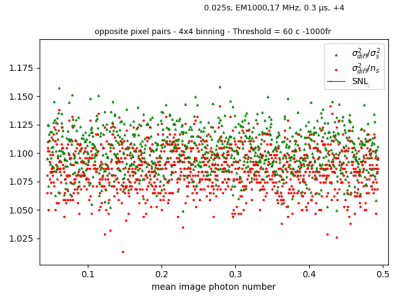

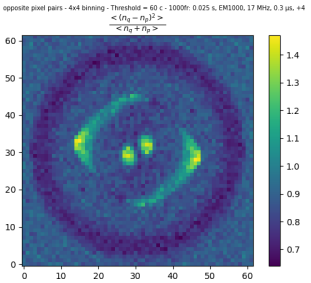

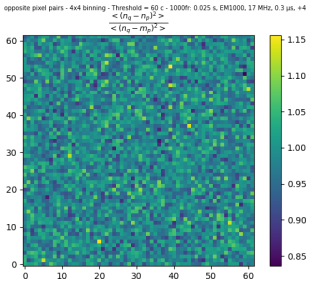

CHAPTER 7

Conclusion and Outlook

In this thesis, I presented the necessary theoretical background for the aimed analysis. Employing my analysis, I found that it is possible to measure sub-shotnoise noise statistics in photon counting mode even in the case where the coherence area is double than the pixel size, while should be at least equal size if not half, by artificially increasing it with binning the pixel in post-process analysis. There, one should be careful on how is treating the photon number, i.e. still binary or 'true' photons, because in the first case especially when considering small sectors the photon number will be practically constant and smaller than the sector size with variance smaller than the mean photon number, hence giving a bigger value for correlation.

I found that larger exposures in the thresholding mode give better correlations because the true photon pairs are better distinguished among the governing CIC noise, assuming proper thresholding to avoid double coincidences.

The three different thresholding calculation I implemented for the same exposure and give the same threshold. The noise statistics derived from the two was slightly different, with the Matfile convolution to overestimate the CIC and the readout noise compared to the analytical calculation. With certainty I can say that the graphical representation was the least painful of all, plus providing the ability of choosing the threshold according to the exposure time wished.

Some correlation between the stray light and the SPDC emission is introduced by the fluctuation of the pump, since when the pump pulse is more or less energetic, both the SPDC and the stray light increase or decrease accordingly. These correlations should cancel out in the photon number difference though if the optical path is optimized properly.

The large statistical sample of 1000 frames seems to not influence the final uncertainty of the mean values, it lowers the mean error of measurement though because of the decrease of the standard deviation.

The superpixel size used for the measurement must realize a trade-off between the visibility of the correlation and the final uncertainty in the center determination. To increase the visibility of the quantum correlation the superpixel area must be much greater than A_{coh}. On the other side a small pixel size leads to a small uncertainty. The best choice is the size equal to the coherence area. Even a shift of a small fraction of a superpixel with respect to the real center determines an increasing of the noise reduction factor. The bigger the super-pixel the larger the uncertainty in the evaluation of the symmetry center, even when this is retrieved by using a superpixel algorithm, as mentioned in references.

I finally conclude that the key to sub-shot noise correlations observation is a precise estimation of the coherence area and an accurate positioning of the array/sensor with respect to the physical center of symmetry, along with the correct thresholding procedure.

Possible improvements and exploration: in binned data treat the super pixel as binary based on if they are non zero or not. (assuming only opposite pixels either sectors, probably would give even more accurate results.)

Bibliography

[1] Andor hardware guide.

[2] Michael Hirsch, Richard J. Wareham, Marisa L. Martin-Fernandez, Michael P. Hobson, and Daniel J. Rolfe. A stochastic model for electron multiplication charge-coupled devices – from theory to practice. *PLoS ONE*, 8(1), 2013.

[3] Kennet Bomann West Harpsoe, Michael Ingemann Andersen, and Per Kjargaard Rasmussen. Bayesian photon counting with electron-multiplying charge coupled devices (emccds). *Astronomy and Astrophysics Supplement Series*, 537, 2012.

[4] Peter Seitz. *Fundamentals of Noise in Optoelectronics*, volume 160, pages 1–25. 08 2011.

[5] Roger J. Barlow. *Statistics: A guide to the use of statistical methods in the Physical Sciences R.J. Barlow*. J. Wiley, 1989.

[6] Olivier Daigle, Oleg Djazovski, Denis Laurin, René Doyon, and Etienne Artigau. Characterization results of emccds for extreme low-light imaging. *High Energy, Optical, and Infrared Detectors for Astronomy V*, 2012.

[7] ccd blemishes and non-uniformities. https://andor.oxinst.com/learning/view/article/ccd-blemishes-and-non-uniformities.

[8] Suman Karan, Shaurya Aarav, Homanga Bharadhwaj, Lavanya Taneja, Arinjoy De, Girish Kulkarni, Nilakantha Meher, and Anand K Jha. Phase matching in β-barium borate crystals for spontaneous parametric down-conversion. *Journal of Optics*, 22(8):083501, jun 2020.

[9] Couteau Christophe. Spontaneous parametric down-conversion, 2018.

[10] Birefringence, 2023.

[11] CARL GROSSMAN. Phase matching in bbo for parametric downconversion of 405 nm light.

[12] Bhaskar Kanseri and Preeti Sharma. Effect of partially coherent pump on the spatial and spectral profiles of down-converted photons. *Journal of The Optical Society of America B-optical Physics*, 37:505–512, 2020.

[13] Jong-Chan Lee and Yoon-Ho Kim. Spatial and spectral properties of entangled photons from spontaneous parametric down-conversion with a focused pump. *Optics Communications*, 366:442–450, 2016.

[14] Lijian Zhang, Leonardo Neves, Jeff S Lundeen, and Ian A Walmsley. A characterization of the single-photon sensitivity of an electron multiplying charge-coupled device. *Journal of Physics B: Atomic, Molecular and Optical Physics*, 42(11):114011, 2009.

[15] E. Brambilla, A. Gatti, M. Bache, and L. A. Lugiato. Simultaneous near-field and far-field spatial quantum correlations in the high-gain regime of parametric down-conversion. *Phys. Rev. A*, 69, 2004.

[16] T. S. LARCHUK, M. C. TEICH, and B. E. SALEH. Statistics of entangled-photon coincidences in parametric downconversiona. *Annals of the New York Academy of Sciences*, 755(1):680–686.

[17] Eric Lantz, Paul-Antoine Moreau, and Fabrice Devaux. Optimising the signal-to-noise ratio in measurement of photon pairs with detector arrays. *arXiv.org ¿ quant-ph ¿ arXiv:1407.2455*, 90, 2014.

[18] Eric Lantz, Severine Denis, Paul-Antoine Moreau, and Fabrice Devaux. Einstein-podolsky-rosen paradox in single pairs of images. *Optics Express*, 23(20):26472, 2015.

[19] Ermes Toninelli, Matthew P. Edgar, Paul-Antoine Moreau, Graham M. Gibson, Giles D. Hammond, and Miles J. Padgett. Sub-shot-noise shadow sensing with quantum correlations. *Optics Express*, 25(18):21826, 2017.

[20] Eric Lantz, Severine Denis, Paul-Antoine Moreau, and Fabrice Devaux. Einstein-podolsky-rosen paradox in single pairs of images. *Optics Express*, 23(20):26472, 2015.

[21] Jean-Luc Blanchet, Fabrice Devaux, Luca Furfaro, and Eric Lantz. Measurement of sub-shot-noise correlations of spatial fluctuations in the photon-counting regime. *Physical Review Letters*, 101(23), 2008.

[22] Eric Lantz, Jean-Luc Blanchet, Luca Furfaro, and Fabrice Devaux. Multi-imaging and bayesian estimation for photon counting with emccds. *Monthly Notices of the Royal Astronomical Society*.

[23] Ottavia Jedrkiewicz, Jean-Luc Blanchet, Eric Lantz, and Paolo Di Trapani. Graphical thresholding procedure and optimal light level estimation for spatially resolved photon counting with emccds. *Optics Communications*, 285(3):218–224, 2012.

[24] Nassim Rousset, Jeremie Villeneuve, Jean-Hughes Fournier Lupien, Anis Attiaoui, Gabriel Taillon, Sebastien Francoeur, and Olivier Daigle. Comparison of emccd post-processing methods for photon counting flux ranges. volume 9154, 2014.

[25] Hugo Defienne, Matthew Reichert, and Jason W. Fleischer. General model of photon-pair detection with an image sensor. *Phys. Rev. Lett.*, 120:203604, 2018.

[26] Eliot Bolduc, Daniele Faccio, and Jonathan Leach. Acquisition of multiple photon pairs with an emccd camera. *Journal of Optics*, 19(5):054006, 2017.

[27] Giorgio Brida, I. Degiovanni, Marco Genovese, Maria Rastello, and Ivano Ruo Berchera. Detection of multimode spatial correlation in pdc and application to the absolute calibration of a ccd camera. *Optics express*, 18:20572–84, 2010.

[28] Sumant Oemrawsingh, Wouter van Drunen, Eric Eliel, and J. Woerdman. Two-dimensional wave-vector correlations in spontaneous parametric downconversion explored with an intensified ccd camera. *JOSA B*, 19:2391–2395, 2002.

[29] Kayn A. Forbes, Jack S. Ford, and David L. Andrews. Nonlocalized generation of correlated photon pairs in degenerate down-conversion. *Phys. Rev. Lett.*, 118:133602, 2017.

[30] Olivier Daigle, Pierre-Olivier Quirion, and Simon Lessard. The darkest emccd ever. In Andrew D. Holland and David A. Dorn, editors, *High Energy, Optical, and Infrared Detectors for Astronomy IV*, volume 7742, page 774203. International Society for Optics and Photonics, SPIE, 2010.

[31] Derek Ives, Naidu Bezawada, Vik Dhillon, and Tom Marsh. Ultraspec - an electron multiplication ccd camera for very low light level high speed astronomical spectrometry. *Proceedings of SPIE - The International Society for Optical Engineering*, 7021, 08 2008.

[32] Olivier Daigle and Sebastien Blais-Ouellette. Photon counting with an emccd. *SPIE Proceedings*, 2010.

[33] A. Meda, I. Ruo-Berchera, I. P. Degiovanni, G. Brida, M. L. Rastello, and M. Genovese. Absolute calibration of a charge-coupled device camera with twin beams. *Applied Physics Letters*, 105(10), 2014.

[34] Giorgio Brida, Lucia Caspani, Alessandra Gatti, Marco Genovese, Alice Meda, and Ivano Ruo Berchera. Measurement of sub-shot-noise spatial correlations without background subtraction. *Physical Review Letters*, 102(21), 2009.

[35] understanding read noise in scmos-cameras. https://andor.oxinst.com/learning/view/article/understanding-read-noise-in-scmos-cameras.

[36] emccd: separating the facts from the fiction. https://andor.oxinst.com/learning/view/article/emccd-separating-the-facts-from-the-fiction.

[37] dynamic range in emccds. https://andor.oxinst.com/learning/view/article/dynamic-range-emccds.

[38] Sensitivity-andor. https://andor.oxinst.com/learning/view/article/sensitivity.

Appendix

APPENDIX A

Appendix

This appendix presents the tables of values obtained from the analysis treating the individual photon number inside the mask as 1 and as non-zero.

Table A.1: Counting as non-zeros

bin-ning	expos-ure	sectors				
		4	90	120	180	
none	0.010	r' =4.13 (±1.75 /0.06) r = 4.48 (±4.28 /0.14)	r' =2.02 (±0.30 /0.01) r = 1.83 (±0.39 /0.01)	r' =2.01 (±0.26 /0.01) r = 1.82 (±0.34 /0.01)	r' =2.01 (±0.22 /0.01) r = 1.80 (±0.27 /0.01)	
	0.015	r' =4.33 (±1.66 /0.05) r = 5.25 (±4.89 /0.15)	r' =2.02 (±0.30 /0.01) r = 1.75 (±0.38 /0.01)	r' =2.00 (±0.26 /0.01) r = 1.74 (±0.31 /0.01)	r' =2.00 (±0.21 /0.01) r = 1.71 (±0.26 /0.01)	
	0.025	r' =4.56 (±1.54 /0.05) r = 5.96 (±5.15 /0.16)	r' =2.01 (±0.30 /0.01) r = 1.63 (±0.35 /0.01)	r' =1.99 (±0.26 /0.01) r = 1.62 (±0.30 /0.01)	r' =1.99 (±0.21 /0.01) r = 1.58 (±0.23 /0.01)	
2x2	0.010	r' =4.08 (±1.77 /0.06) r = 2.78 (±2.76 /0.09)	r' =1.98 (±0.30 /0.01) r = 1.26 (±0.27 /0.01)	r' =1.99 (±0.26 /0.01) r = 1.26 (±0.24 /0.01)	r' =1.95 (±0.21 /0.01) r = 1.33 (±0.20 /0.01)	
	0.015	r' =4.12 (±1.77 /0.06) r = 2.39 (±2.20 /0.07)	r' =1.93 (±0.31 /0.01) r = 1.04 (±0.22 /0.01)	r' =1.96 (±0.27 /0.01) r = 1.05 (±0.20 /0.01)	r' =1.88 (±0.22 /0.01) r = 1.09 (±0.16 /0.01)	
	0.025	r' =4.26 (±1.66 /0.05) r = 1.84 (±1.80 /0.06)	r' =1.86 (±0.31 /0.01) r = 0.77 (±0.17 /0.01)	r' =1.92 (±0.27 /0.01) r = 0.78 (±0.15 /0)	r' =1.76 (±0.21 /0.01) r = 0.75 (±0.19 /0)	

4x4	0.010	r' =3.99 (±1.77 /0.06) r = 0.61 (±0.62 /0.02)	r' =1.24 (±0.26 /0.01) r = 0.30 (±0.08 /0)	r' =0.96 (±0.20 /0.01) r = 0.32 (±0.08 /0)	r' =1.14 (±0.20 /0.01) r = 0.30 (±0.07 /0)	
	0.015	r' =4.07 (±1.74 /0.06) r = 0.32 (±0.34 /0.01)	r' =0.85 (±0.21 /0.01) r = 0.15 (±0.05 /0)	r' =0.62 (±0.15 /0) r = 0.17 (±0.05 /0)	r' =0.75 (±0.17 /0.01) r = 0.15 (±0.04 /0)	
	0.025	r' =nan r = 0.10 (±0.11 /0)	r' =0.34 (±0.12 /0) r = 0.04 (±0.02 /0)	r' =0.29 (±0.08 /0) r = 0.07 (±0.02 /0)	r' =0.29 (±0.10 /0) r = 0.04 (±0.02 /0)	

Table A.2: Counting as integer numbers

bin-ning	expos-ure	sectors				
		4	90	120	180	
none	0.010	r' =4.13 (±1.75 /0.06) r = 4.48 (±4.28 /0.14)	r' =2.02 (±0.30 /0.01) r = 1.83 (±0.39 /0.01)	r' =2.01 (±0.26 /0.01) r = 1.82 (±0.34 /0.01)	r' =2.01 (±0.22 /0.01) r = 1.80 (±0.27 /0.01)	
	0.015	r' =4.33 (±1.66 /0.05) r = 5.25 (±4.89 /0.15)	r' =2.02 (±0.30 /0.01) r = 1.75 (±0.38 /0.01)	r' =2.00 (±0.26 /0.01) r = 1.74 (±0.31 /0.01)	r' =2.00 (±0.21 /0.01) r = 1.71 (±0.26 /0.01)	
	0.025	r' =4.56 (±1.54 /0.05) r = 5.96 (±5.15 /0.16)	r' =2.01 (±0.30 /0.01) r = 1.63 (±0.35 /0.01)	r' =1.99 (±0.26 /0.01) r = 1.62 (±0.30 /0.01)	r' =1.99 (±0.21 /0.01) r = 1.58 (±0.23 /0.01)	
2x2	0.010	r' =4.49 (±1.54 /0.05) r = 5.43 (±4.83 /0.15)	r' =1.98 (±0.31 /0.01) r = 1.83 (±0.39 /0.01)	r' =1.97(±0.26 /0.01) r = 1.82 (±0.34 /0.01)	r' =1.96 (±0.22 /0.01) r = 1.80 (±0.27 /0.01)	
	0.015	r' =4.27 (±1.68 /0.05) r = 4.76 (±4.53 /0.14)	r' =1.95 (±0.31 /0.01) r = 1.75 (±0.38 /0.01)	r' =1.95 (±0.26 /0.01) r = 1.75 (±0.32 /0.01)	r' =1.91 (±0.22 /0.01) r = 1.72 (±0.26 /0.01)	
	0.025	r' =4.49 (±1.54 /0.05) r = 5.43 (±4.83 /0.02)	r' =1.89 (±0.31 /0.01) r = 1.57 (±0.33 /0.01)	r' =1.90 (±0.26 /0.01) r = 1.58 (±0.29 /0.01)	r' =1.85 (±0.21 /0.01) r = 1.52 (±0.23 /0.01)	

4x4	0.010	r' =4.13 (±3.90 /0.12) r = 4.12 (±1.74 /0.06)	r' =1.83 (±0.40 /0.01) r = 1.67 (±0.30 /0.01)	r' =1.87 (±0.36 /0.01) r = 1.46 (±0.25 /0.01)	r' =1.80 (±0.29 /0.01) r = 1.61 (±0.22 /0.01)	
	0.015	r' =4.53 (±4.44 /0.14) r = 4.19 (±1.72 /0.05)	r' =1.76 (±0.38 /0.01) r = 1.55 (±0.29 /0.01)	r' =1.81 (±0.33 /0.01) r = 1.32 (±0.25 /0.01)	r' =1.72 (±0.27 /0.01) r = 1.48 (±0.21 /0.01)	
	0.025	r' =5.15 (±4.70 /0.15) r = 4.38 (±1.61 /0.05)	r' =1.58 (±0.34 /0.01) r = 1.31 (±0.25 /0.01)	r' =1.67 (±0.30 /0.01) r = 1.05 (±0.20 /0.01)	r' =1.54 (±0.24 /0.01) r = 1.23 (±0.19 /0.01)	

APPENDIX B

Acknowledgements

I would like to thank anyone that helped me throughout my thesis conduction, but especially Prof Frank Vewinger for his precious help in fixing a functioning setup, providing equipment and guidance. Further, Mr Wolfgang ALt for his fruitful insides and triggering questions for thought.